Draft version September 25, 2023
Typeset using LaTeX **twocolumn** style in AASTeX631

Flares hunting in hot subdwarf and white dwarf stars from the 1-4 cycles of TESS photometry

Keyu Xing[1,2] and et al.

[1] *Institute for Frontiers in Astronomy and Astrophysics, Beijing Normal University, Beijing 102206, P. R. China*
[2] *Department of Astronomy, Beijing Normal University, Beijing 100875, P. R. China*

ABSTRACT

Stellar flares are critical phenomena on stellar surfaces, which are closely tied to stellar magnetism. While extensively studied in main-sequence stars, their occurrence in evolved compact stars, specifically hot subdwarfs (HSDs) and white dwarfs (WDs), has been scarcely explored, largely due to their faint brightness, weak magnetic fields and complex variability. Based on the 1-4 cycles of TESS photometry, we conducted a pioneering survey of flare events in over 11 000 compact stars, corresponding to ∼31 000 light curves with 2-minute cadence. We developed dedicated techniques for detrending light curves, identifying preliminary flare candidates, and validating these candidates through a machine learning algorithm. After extensive vetting, we established a catalog of 960 flares originated from 190 compact stars, including 172 from 59 HSDs and 788 from 131 WDs. Further refinement accounting for potential contamination yielded a clean sample of 65 HSD and 24 WD flares. Our results indicate that flares in WDs exhibit higher amplitudes than those in HSDs, which may be linked to stronger magnetism in WDs. The flare characteristics imply an analogous origin between HSDs and early B/A-type stars. This comprehensive catalog provides unprecedented insights into flare activities in compact stars and lays a robust foundation for future magnetism studies in evolved stellar objects.

Keywords: Compact star — Photometry — Stellar Flare — Machine Learning — Random Forest

1. INTRODUCTION

Stellar flares are abrupt, intense phenomena that manifest as a rapid increase in luminosity across a broad wavelength coverage, from radio to gamma-ray (Benz & Güdel 2010). These flares can be orders of magnitude more energetic than their solar counterparts, and such intensity can have significant implications for the habitability of orbiting exoplanets (e.g., Vida et al. 2017). The underlying mechanisms that generate stellar flares are believed to be analogous to those of solar flares (Davenport 2016).

Flares are believed to be closely related to magnetic activity on stellar surfaces. They are triggered by the sudden release of magnetic energy through the reconnection of twisted magnetic field lines within the stellar atmosphere. In cool main-sequence (MS) stars, these magnetic fields arise from dynamo processes occurring within their convective envelopes, whose depth is a critical factor determining the level of stellar magnetic activity (Charbonneau 2010). In particular, stars with deeper convective layers are capable of generating more robust dynamo mechanisms, leading to stronger surface magnetic fields and higher frequencies of flares. This relationship manifests as an observed trend where the incidence of flare stars increases progressively from F-type to M-type main-sequence stars (Yang & Liu 2019).

Incapable of resolving details of stellar surfaces, studies of stellar flares rely on time-resolved photometric or spectroscopic observations (Walkowicz et al. 2011). Before the era of space-borne photometry, various types of observations of flares, for instance, radio waves (Bastian et al. 1988), X-rays (Schmitt et al. 1993), and spectroscopy (Pettersen & Hawley 1989), offer different insights to their properties but lacking in continuous data coverage for their temporal evolution. While time-resolved spectroscopy enables detailed plasma diagnostics and detection of mass ejections of single flare events (e.g. Namekata et al. 2021), continuous photometric monitoring provides a broader view, allowing for statistical analyses of flare frequencies and energies over extended periods. The Kepler, K2, and TESS missions (Koch et al. 2010; Howell et al. 2014; Ricker et al. 2014),

weikai.zong@bnu.edu.cn

collecting high-quality and long consecutive photometry, have fertilized the field of flare studies, exposing various properties and correlations of flares to their hosting stellar types across the HR diagram (e.g., Davenport 2016; Günther et al. 2020; Yang et al. 2023).

Despite these advances, the knowledge of flare to evolved compact stars, specifically hot subdwarfs and white dwarfs, remains very limited. Hot subdwarfs (HSDs), burning helium in the core with a thin hydrogen envelope, are stars located at the blue end of the horizontal branch, also known as the extreme horizontal branch (Heber 2009). White dwarfs (WDs) are remnants of $\sim 97\%$ stars in the Milky Way when they cease nuclear fusion, resulting in a degenerate core typically composed of carbon and oxygen and cooling down for the rest of their lives (Saumon et al. 2022). Contrary to cool MS stars, hot compact stars do not present deep convective envelopes, which prevents the twist of magnetic field lines through dynamo processes, although strong magnetism has been claimed in HSDs and WDs (Bagnulo & Landstreet 2021; Vos et al. 2021; Pelisoli et al. 2022). Therefore, whether these magnetic compact stars can present flare event is an open interesting question to understand the mechanism between flare and magnetism.

However, it is a challenge to search for flare events in HSD and WD stars since their sample is relatively small due to their brightness and flare hunting needs intensive photometric monitoring. The current HSD and WD candidates are found about 7000 (see, e.g., Culpan et al. 2022) and 360 000 (see, e.g., Gentile Fusillo et al. 2021), respectively. TESS mission provides the first opportunity for such research as it collected extensive photometry for a large fraction of HSD and WD stars brighter than $G < 16$ (Charpinet et al. 2019; Ricker et al. 2014). It attracts intensive attention to investigate various types of brightness variation in those compact stars, for instance, brightness modulation from different binary effects (see, e.g., Schaffenroth et al. 2022) and rapid variation from gravity and pressure pulsations (see, e.g., Romero et al. 2022; Baran et al. 2023). As offered by TESS photometry, we initiate the pioneering survey with an aim that tries to find flare events in HSD and WD stars.

In line with this study, light curves of compact stars may present complex variability which brings difficulty in flare identification. For instance, Pietras et al. (2022) excluded stars with spectral types earlier than F1 due to their diverse and rapid brightness variation that resemble stellar flares. Therefore, detrending the light curves of compact variable stars correctly and distinguishing intrinsic flares from other transient events requires dedicated techniques for flare identification and validation. Although there are several existing practices to detecting flare events automatically (e.g. Davenport 2016; Doorsselaere et al. 2017; Günther et al. 2020; Ilin et al. 2021), they generally rely on simple outlier detection in flattened light curves without considering event morphology. As a result, they struggle to distinguish flares from artifacts or other rapid brightening events. Yang & Liu (2019) found serious contamination of previous flare catalogs by various pulsators, rapid rotators, and transits. Other methods for detecting flares rely on machine learning algorithms (e.g., Feinstein et al. 2020), but these may perform poorly when analyzing light curves with fast and complex brightness modulations.

The rest of this paper is structured as follows. In Section 2, we describe the TESS photometry collected on our concerning compact stars. Section 3 provides details of our methods for preliminary identification of flare candidates, including a new approach designed to address short-term periodic variations that enhances our ability to identify flares in compact stars. We also describe several indispensable steps to exclude contamination from cataclysmic variables and solar system objects. Section 4 then explains our process to validate the preliminary candidates using a Random Forest classifier trained on a series of simulated data. We present the resulting flare catalog and analyze the properties of these events in Section 5, also considering potential contamination and establishing a refined sample of compact stars. Finally, Section 6 provides a summary of our results and a discussion of their implications regarding flare production mechanisms in compact stars.

2. TESS PHOTOMETRY

The Transiting Exoplanet Survey Satellite (TESS; Ricker et al. 2014) was launched on 18 April 2018, and began observing in July 2018. After completing the primary mission in July 2020 and the first extended mission in September 2022, TESS is currently conducting its second extended mission, which will last approximately three years. Both the primary mission and the first extended mission consist of two cycles of observations. The southern ecliptic hemisphere was observed in Cycle 1 and 3, whereas the northern ecliptic hemisphere was observed in Cycle 2 and 4. Each cycle is composed of 13 sectors, except for Cycle 4 which has 16 sectors. Each sector covers a $24^\circ \times 96^\circ$ strip of the sky and is observed for a period of $\sim$27 d, with an angular resolution of 21 arcsec pixel^{-1}. Due to the overlaps among the sectors in each cycle, a portion of TESS targets were observed multiple times during the survey. Targets in the

Table 1. The observed sectors of the compact stars by TESS in Cycle 1-4.

Sectors	Targets	Light curves
1	4370	4370
2	3230	6460
3	1492	4476
4	764	3056
5	326	1630
$\geqslant 6$	911	10855
Total	11093	30847

vicinity of the ecliptic poles were observed continuously for almost one year.

TESS is equipped with four 10.5 cm optical telescopes and four identical cameras having a red bandpass covering the wavelength range from 600 nm to 1000 nm. Each camera has a field of view of 24° × 24° and consists of four 2 k×2 k back-illuminated CCDs, which continuously read out at 2-second intervals for spacecraft guiding. These 2-second data are then stacked, compressed, and stored on the spacecraft until TESS reaches its perigee after every 13.7-day orbital period, at which point TESS downlinks the collected data to Earth.

During Cycle 1-4 (Sector 1-55), TESS observed 11 093 compact stars, including 7414 white dwarfs and 3679 hot subdwarfs, proposed by the TESS Asteroseismic Science Consortium (TASC)[1] Working Group 8 (WG8), which focuses on variability in evolved compact stars (see, e.g., Charpinet et al. 2019; Bognár et al. 2020). There are 30 847 light curves with 2-minute cadence that have been collected for these compact stars. We retrieve their light curves from the Mikulski Archive for Space Telescopes (MAST)[2], which were processed through the standard pipeline of the Science Processing Operations Center (SPOC) (Jenkins et al. 2016). Table 1 lists the detailed observations of these compact stars: nearly two-thirds of the targets were observed in one or two sectors, while about one-tenth were visited by more than five sectors. We analyze all these 30 847 light curves and characterize flare events using the Pre-search Data Conditioning Simple Aperture Photometry (PDCSAP) flux, where common instrumental systematics has been removed using the co-trending basis vectors. In each light curve, all epochs with quality bit flags equal to 1, 2, 3, 4, 5, 6, 8, 10, 13 and 15 are masked out, which are the recommended quality flags in the TESS Data Product documentation[3].

[1] https://tasoc.dk

[2] https://archive.stsci.edu/tess/bulk_downloads.html

3. FLARE CANDIDATES DETECTION

Flares are shown as consecutive positive outliers in light curves. To detect these outliers, we first detrend the light curves to remove astrophysical variability. Then, we identify groups of outliers in the detrended light curves that meet certain criteria, which are regarded as preliminary flare candidates since their profiles have not yet been considered. We exclude the light curves of known cataclysmic variables (CVs) due to their complexity and irregularity. We also inspect whether each candidate is caused by a solar system object (SSO) encounter event.

3.1. *Detrending algorithm and window length*

For many studies on flare detection, the Savitky-Golay filter (Savitzky & Golay 1964) has been adopted to detrend the light curve by various groups (e.g. Ilin et al. 2021). However, the Savitky-Golay filter is cadence-based, which means that it cannot function as designed on time series with observational gaps, which can be caused by factors such as cosmic rays or satellite attitude tweaks.

Hippke et al. (2019) compared the relative performance of various detrending algorithms for transit discovery. They concluded that, in many cases, it is optimal to use a time-windowed slider with an iterative robust location estimator based on Tukey's biweight (Mosteller & Tukey 1977). This result can also be applied to flare detection since transits and flares are both signals constituting small segments of the light curves. Meanwhile, the Savitky-Golay filter easily overfits the transit signals, which reduces their depth and warps up the detrended light curve around the transit. This will introduce extra outliers and bring some false alarm detection of flares (see Figure 1 & 11 in Hippke et al. 2019). Therefore, instead of using the Savitky-Golay filter, we adopt the biweight filter implemented in `wōtan` (Hippke et al. 2019), an open-source Python package for time-series smoothing, to detrend the light curves.

Next, we need to correctly determine the window length for the biweight filter before detrending. A narrow window can remove the stellar variability effectively but may overfit the large flares, which introduces underestimations of their duration and amplitude, as shown

[3] https://outerspace.stsci.edu/display/TESS/2.0+-+Data+Product+Overview

in Figure 1(b). To avoid overfitting flares, the window length should be several times longer than their durations. A recent work by Howard & MacGregor (2022, hereafter H22) identified 3792 flares from 226 M-dwarfs based on 20-s cadence photometry from TESS Cycle 3, providing the information of the duration of these flares. From their results, we conclude that only 178 flare events, corresponding to $\sim$5 % of the detected flares, have a duration longer than 0.1 d. We thus set the window length to 0.3 d in the application of the biweight filter, which is considerably long enough for the durations of most flares.

3.2. *Detrending procedure*

Flares typically last from minutes to hours, rarely longer than 1 d (Ilin & Poppenhaeger 2022). In some cases, the light curves of compact stars exhibit periodic variations, on a timescale order $\lesssim$1 d, induced by factors such as pulsations or binary effects. Such variations cannot be easily removed if a wide window is chosen to preserve large flares during the detrending process, as shown in Figure 1(a). In addition, it can result in the failure to detect flares with amplitudes comparable to those periodic variations. We thus have to implement an automated procedure for detrending light curves, with a particular focus on identifying and removing these short-term periodic variations.

We firstly normalize the light curves by dividing them by the total median and compute the Lomb-Scargle periodogram (Lomb 1976; Scargle 1982). If the period of the highest peak, P, is in the range of 0.05 d to 2 d and with significant confidence (we arbitrarily adopt 4 times the median noise level), then this light curve will be considered to have short-period variability, otherwise it will be directly detrended with the biweight filter. In some special cases, instead of the period of the maximum power signal, its harmonics represent the true period of brightness variation. Therefore, the light curve will be folded with $P, 2P$ and $4P$, respectively. We then apply a median filter with a sliding window of $P_{\rm fold}/50$ to each folded light curve to generate models of the short-period variability, where $P_{\rm fold}$ is the folded period of the light curve (Figure 2). After evaluating the standard deviations of the residuals of all models, the optimum model will be selected and subtracted from the light curve. Lastly, the differential light curves will be detrended using the biweight filter with a window length of 0.3 d. Both large and small flare profiles are preserved and can be easily detected through this procedure (Figure 3).

3.3. *Removing detached eclipses*

The aforementioned procedure can effectively detrend most light curves, but it fails, in particular, for a few with detached eclipses. The folded models cannot correctly recover the periodic variations because detached eclipsing signals require many harmonics to be represented in Fourier transformation.

To avoid this flaw during the detrending process, we therefore remove the eclipses before applying the biweight filter. The eclipses are masked in the light curve where more than three consecutive epochs are below $-3\sigma_{\rm MAD}$ from the median before subtracting the folded model. Here $\sigma_{\rm MAD}$ is a robust standard deviation calculated using the median absolute deviation (MAD), given by

$$\sigma_{\rm MAD} \approx 1.4826\,{\rm MAD}, \tag{1}$$

assuming that the data is normally distributed (Huber & Ronchetti 1981). We then extend each masked segment on both sides until an epoch is above the median of the light curve, ensuring the entire eclipse is covered (Figure 2).

3.4. *Searching for flare candidates*

After detrending the light curve, we slide a 2-day window along it and calculate its rolling $\sigma_{\rm MAD}$ to estimate the local noise level. We then standardize the light curve by

$$F_{\rm standardized} = \frac{F_{\rm detrended} - 1}{\sigma_{\rm MAD,\,rolling}}, \tag{2}$$

where $F_{\rm detrended}$ is the normalized detrended light curve, $\sigma_{\rm MAD,\,rolling}$ is the rolling $\sigma_{\rm MAD}$ and $F_{\rm standardized}$ is the standardized light curve. Standardization is a technique that transforms data to have a mean of 0 and a standard deviation of 1, commonly used when datasets have varying scales. In this case, we use standardized light curves, which represent the deviation of the flux measurements from the median in units of rolling $\sigma_{\rm MAD}$, to simplify identifying and validating preliminary flare candidates in subsequent analyses.

To identify groups of outliers as preliminary flare candidates, we search for at least N_1 consecutive measurements above $N_2 \times \sigma$ from the median, i.e., greater than N_2 in the standardized light curve. Lower values of $N_{1,2}$ recover more low-amplitude flares but increase the number of false positives due to artifacts, and vice versa. We empirically select a threshold of $N_1 = 2$ and $N_2 = 3$, compromising between the efficiency of recovering flare events and minimizing false positives.

Although the above criteria are sufficient for identifying flare candidates, the start of their rising phases and the end of their decaying phases may be cut off if they lie below the 3σ threshold. We therefore extend the profiles of flare candidates, similar to the extension process

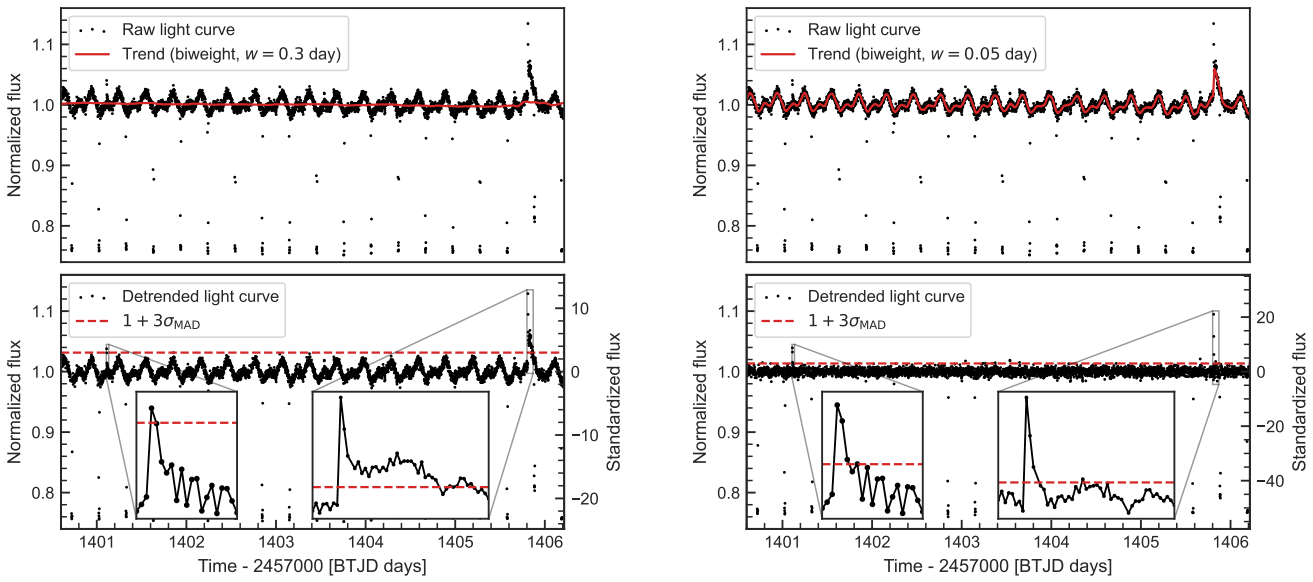

Figure 1. Detrending the light curve of TIC 219244444 (RR Cae, a white dwarf eclipsed by an M-dwarf every ∼0.3 d; Maxted et al. 2007) in TESS Sector 3 using the biweight filter with two different window lengths: (a) long of 0.3 d, (b) short of 0.05 d. Top: raw flux (black points) and trend flux (red solid line). Bottom: detrended flux (black points), $3\sigma_{\rm MAD}$ from the median (red dashed line) and zoom windows of one small flare (left) and one large flare (right). The large flare is overfitted with the short window, while the small flare cannot be detected with the long window. Only a segment of the light curve is shown in this figure.

in Section 3.3, to provide a more accurate estimation of their parameters. Considering the rapid rise and gradual decay of flare events, we extend the left and right sides of each candidate event until one and two consecutive epochs, respectively, fall below $\sigma_{\rm MAD}$ from the median, i.e., less than 1 in the standardized light curve.

3.5. *Rejection of CVs and SSO encounters*

Cataclysmic variables (CVs) have also been proposed in the TESS WG8 target list as they consist of a white dwarf primary and a mass transferring secondary. However, it is difficult to identify flare events in the light curves of CVs since they exhibit rich variable properties across different time scales from seconds to millennia (Bruch 2022). The majority of outbursts are not triggered by flare events (e.g. superhumps), leading to severe pollution in our identification. We thus have to disregard those light curves by querying the type of each compact star from the SIMBAD astronomical database[4] (Wenger et al. 2000).

When a small, foreground solar system object (SSO) (e.g. asteroid, comet) moves across the aperture mask of a target, it tends to cause a symmetrical profile of increasing flux on the light curve as shown in Figure 4. This phenomenon has been extensively discussed by Pál et al. (2018). The SSO encounter events can be easily misidentified as flare candidates and hence need to be excluded. We use the SkyBoT[5] service (Berthier et al. 2006) to identify the false signals caused by SSO encounters, which has been practiced in the *Kepler*/*K2* images (Berthier et al. 2016). For each flare candidate, we perform a cone search in SkyBoT with a radius of 8 TESS pixels, corresponding to 2.8′, at the peak time, which returns a list of known SSOs located in the vicinity of the target. However, if a SSO is very faint, it will have little impact on the light curve even if it is identified with flare events (see e.g. Günther et al. 2020). As a result, we also query the visual magnitude of the SSOs from the JPL Horizons system[6] (Giorgini et al. 2001) and remove those fainter than 19 $V_{\rm mag}$, which will retain the real flares occurring on the targets passing by faint SSOs.

4. FLARE CANDIDATES VALIDATION

[4] https://simbad.cds.unistra.fr/simbad/

[5] https://vo.imcce.fr/webservices/skybot/

[6] https://ssd.jpl.nasa.gov/horizons/

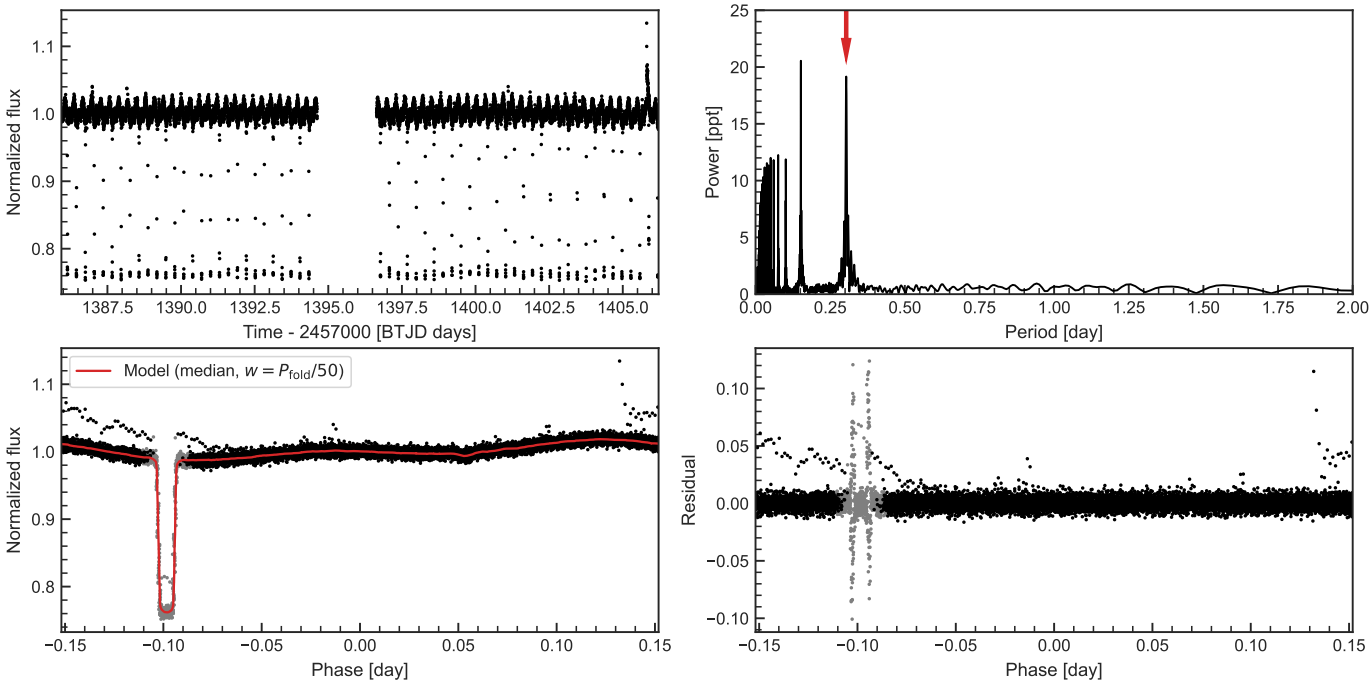

Figure 2. An example of generating the model of the short-period variability in the light curve of TIC 219244444. Top: the light curve of TIC 219244444 in TESS Sector 3 (left) and its Lomb–Scargle periodogram (right). The red arrow indicates the period used to fold the light curve ($P_{\rm fold} = 0.304$ d), which is twice the period at the max power. Bottom: the folded light curve and its model (red solid line) obtained by applying the median filter (left) and the residual of the model (right). The epochs masked by the processing in Section 3.3 are marked with grey points. The model fits the short-period variability well except the ingress and egress of the eclipse.

While the criteria described above are effective in identifying preliminary flare candidates, they may also capture other types of transient events or artifacts, resulting in a considerable number of false positives. Despite our efforts to minimize them through the aforementioned steps, some non-flare events may still exist due to various reasons such as poor data quality, uncategorized CVs in SIMBAD, and targets affected by unknown SSOs. As a result, a more rigorous validation process is required to eliminate non-flare events from the preliminary flare candidates.

Owing to the substantial number of preliminary candidates, we adopt Random Forest (RF; Breiman 2001), a supervised machine learning algorithm, to automatically evaluate the confidence level of each candidate. We generate batches of flare and non-flare events through a series of simulations, which serve as the training inputs for the RF classifier. The classifier then evaluates each candidate and calculates a confidence probability for it being an intrinsic flare event. Candidates with a probability that exceeds a certain confidential threshold are accepted as validated candidates.

4.1. *Random Forest*

Random Forest (RF) is an ensemble machine learning method that can be used for both regression and classification problems. It is constructed by combining multiple decision trees, with each tree being trained on a different subsample of the training set generated by bootstrap aggregation, also known as bagging (Breiman 1996). For classification tasks, the RF classifier outputs the class probabilities of an input sample by averaging the predicted class probabilities from each tree in the forest. Unlike a single decision tree, which can be unstable and sensitive to noise, RF combines the results of numerous weakly correlated trees, providing more accurate and robust predictions.

Due to its high accuracy, low variance and ease of application, RF has been widely used for various classification tasks (e.g. Brink et al. 2013; Wyrzykowski et al. 2015; Wyrzykowski et al. 2016; Godines et al. 2019). Previous literature has also reported that RF outperforms other machine learning methods when classifying variable stars (see, e.g., Richards et al. 2011; Brink et al. 2013; Pashchenko et al. 2017). Given these successful applications and outstanding performance in comparisons, we choose to apply RF to validate the preliminary flare candidates. For this research, we use `scikit-learn` (Pedregosa et al. 2011), an open source

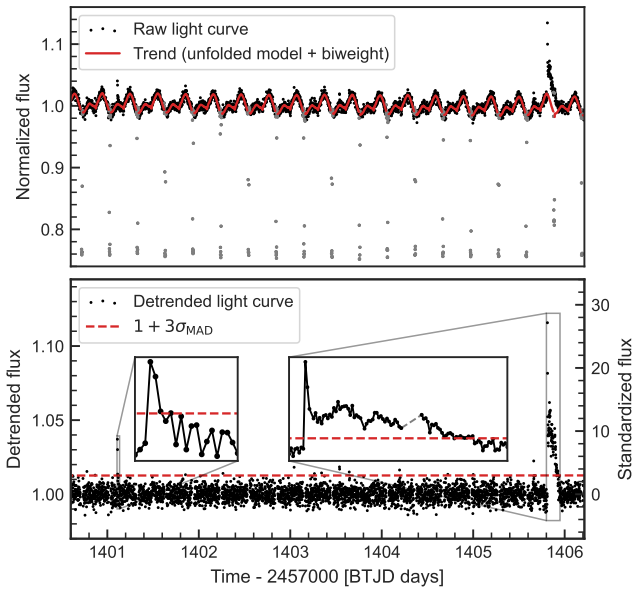

Figure 3. The same with Figure 1, but using our detrending procedure instead of directly using the biweight filter. The trend flux (red solid line) is the combination of the unfolded model of the short-period variability and the trend flux obtained using the biweight filter afterwards. The grey points in the top panel are removed (see Section 3.3) in the detrended light curve, which causes the missing data (grey dashed line) in the right zoom window of the bottom panel.

Python package for machine learning, to build the RF classifier.

4.2. *Training set*

As a supervised learning method, RF requires a training set that is composed of objects with known labels. We choose to construct the training set from simulations rather than relying on data from previous surveys. Using simulations enables the creation of a comprehensive and accurate training set with minimal label contamination because it allows for precise control of input parameters and the generation of a broader variety of flare events, which might be underrepresented in previous survey data due to incomplete samples of low-energy flares (Feinstein et al. 2020).

4.2.1. *Flare model*

Davenport et al. (2014) generated an empirical flare template using classical (single peak) flares discovered in all 11 months of 1-minute cadence data for GJ 1243, an active M4 star, available from *Kepler* Data Release 23. This flare template has been widely used for constructing light curves of flare (e.g. Günther et al. 2020). Recently, Mendoza et al. (2022, hereafter M22) reanalyzed the same data for GJ 1243 using the *Kepler* Data Release 25, where the light curve processing was improved. They generated an updated analytic and continuous flare template, addressing the limitations of the flare template in Davenport et al. (2014). We thus adopt the flare template in M22 to generate the simulated flare events here.

The M22 flare template used the convolution of a Gaussian and a double exponential to model the morphology of the flares, which can be parameterized with three variants: amplitude, the full time width at half the maximum of the flux (FWHM, also known as $t_{1/2}$ in Kowalski et al. 2013) and center time (similar to $t_{\rm peak}$ in Davenport et al. 2014, the moment flare peaks). The flare template was normalized to a relative flux scale, ranging from 0 (before and after the flare occurs) to A, the amplitude (at the flare peak). By changing variants of parameters from specific distributions, we can generate various simulated flare events using this flare template.

4.2.2. *Parameters fitting for simulated flares*

To create simulated flares that accurately represent real ones as close as possible, we use observed data to fit the distributions of flare parameters. By drawing parameters from these fitted distributions, we can generate simulated flare events that are statistically representative of real ones. Since the center time does not affect profiles of flare, we completely concentrate on determining the distributions of its amplitude and FWHM.

We specifically choose to use the parameters of the 3792 M-dwarf flares listed in H22, as they provide the photometric signal-to-noise ratio (S/N), $\sigma_{\rm peak}$, of the flare peaks, which corresponds to the amplitude A in the M22 flare template. By using $\sigma_{\rm peak}$ to represent the amplitude, we ensure that the flux of the simulation is directly comparable to the standardized flux of the preliminary flare candidates, which enables us to use the standardized flux as input for the RF classifier without any additional transformation. Additionally, since H22 provides only the rise and decay times of the flares without their FWHM, we apply an approximate method to obtain them. Based on the M22 flare template, the rise time is roughly equal to 0.6×FWHM. We therefore divide the rise time of each flare by 0.6 to estimate the corresponding FWHM for each flare.

We then fit the distributions of the amplitude and FWHM of the flares. In general, a strong correlation happens between the two parameters, i.e., the higher amplitude, the longer FWHM. In H22, the histograms of these two parameters exhibit a skewed distribution with a long tail toward larger values, which is characteristic of log-normal distributions (Figure 5). Since the natural

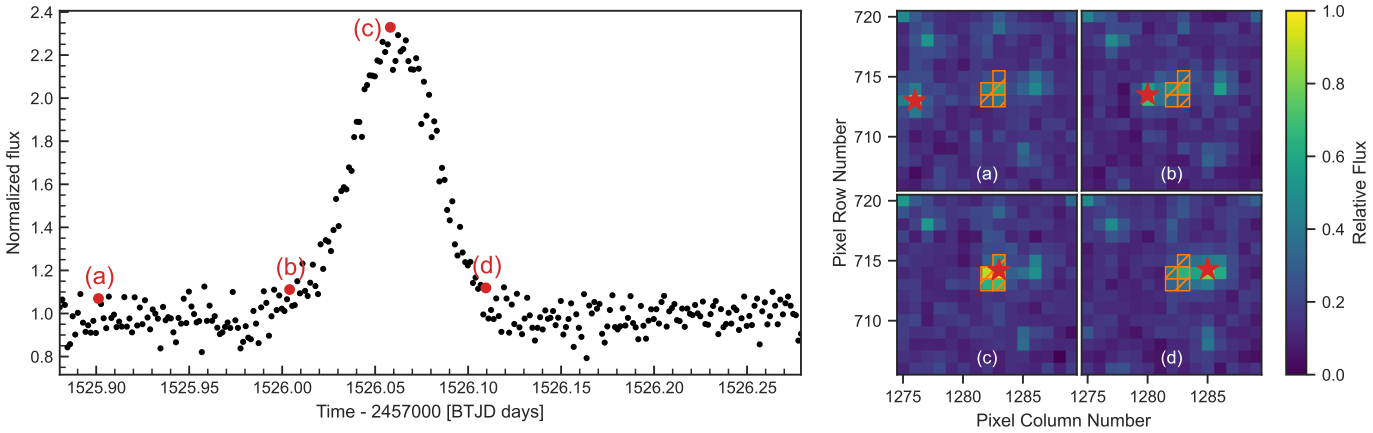

Figure 4. A SSO encounter event found in the light curve of TIC 275308213 in TESS Sector 8. The light curve shown in the left panel is the photometry result using the aperture shown as orange region in the right panel, where presents four frames of the target pixel file during the process that a SSO, marked by red star symbol, encounter the target star. The corresponding fluxes of these moments are also marked in the light curve.

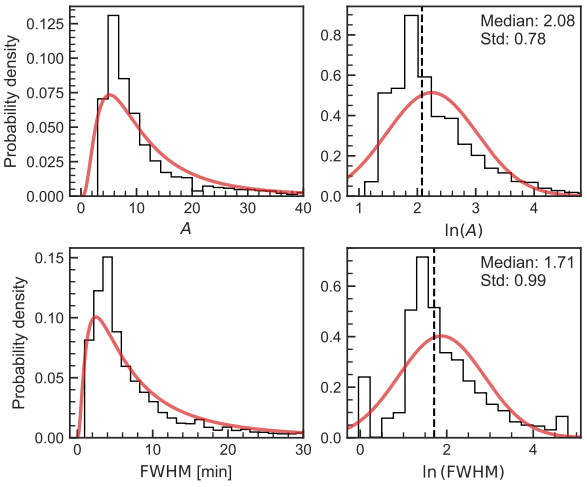

Figure 5. Histograms of the amplitude A and FWHM values, along with their natural logarithm, for the flare samples from H22. Left panels: The distributions of amplitude and FWHM values (black step lines) and the fitted log-normal distributions (red solid lines). Right panels: The distributions of the natural logarithm of amplitude and FWHM values (black step lines) and the fitted normal distributions for the transformed data (red solid lines). The median values, indicated by vertical dashed lines, and standard deviations are provided in the upper right corner of each panel, which are used to initialize the walkers in the emcee analysis.

logarithm of a random variable that is log-normally distributed has a normal distribution, we take the natural logarithm of the amplitude and FWHM values, and then fit a bivariate normal distribution to the transformed data to simplify the fitting process. A bivariate normal distribution is a two-dimensional generalization of the normal distribution, which is parameterized by the means, standard deviations, and correlation coefficient of the two variables. In this case, we fit the means of the natural logarithm of amplitude ($\mu_{\rm A}$) and FWHM ($\mu_{\rm FWHM}$), the standard deviations of the natural logarithm of amplitude ($\sigma_{\rm A}$) and FWHM ($\sigma_{\rm FWHM}$), and the correlation coefficient (ρ) between the natural logarithm of amplitude and FWHM.

We use the Python package `emcee` (Foreman-Mackey et al. 2013) to perform a Markov Chain Monte Carlo (MCMC) analysis for this fit. We initialize the walkers by slightly perturbing the median and standard deviation of the transformed data shown in Figure 5 for the means and standard deviations of the natural logarithm of amplitude and FWHM, and randomly setting the initial correlation coefficient $\rho \in [0, 1]$ for each walker. We ran `emcee` using 128 walkers and 20 000 steps, and discarded the first 2000 steps as burn-in, which is sufficient to reach convergence. The acceptance fraction was 0.551, with a mean auto-correlation time of 51.5 steps. The resulting posterior probability distributions of the five parameters in the bivariate normal distribution, along with their median and 1σ confidence intervals, are displayed in Figure 6.

4.2.3. *Generating the simulated events*

Using the best-fit parameters obtained from the MCMC analysis, we define a bivariate normal distribution to generate paired samples of the natural logarithm of amplitude and FWHM values, which are then input into the M22 flare model to produce a series of simulated flare events. As the flux of these events is standardized, it is essential to introduce noise following a standard normal distribution to create a more realistic representation of the observed data, ensuring that the simulation

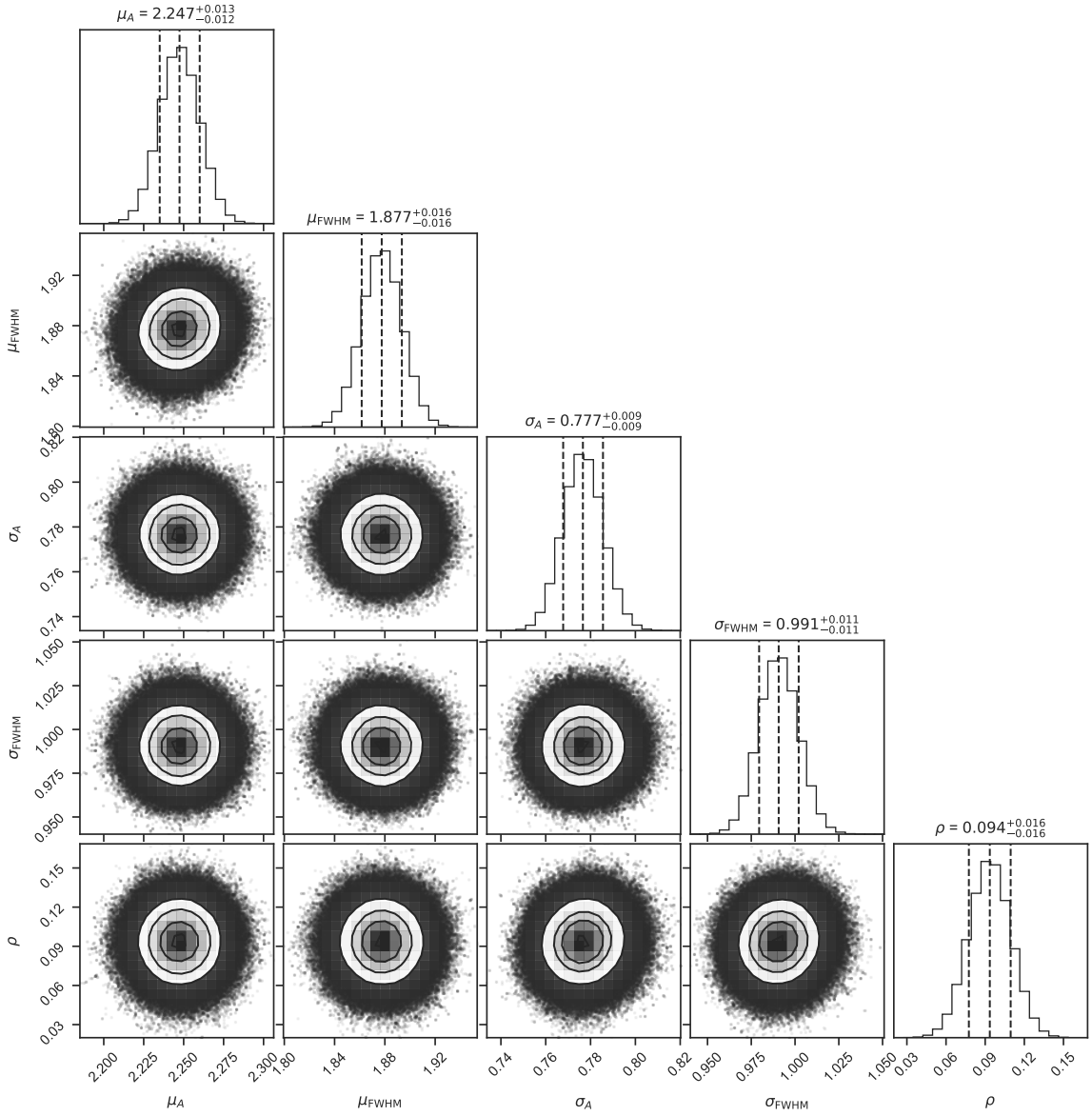

Figure 6. The posterior probability distributions of the five parameters in the bivariate normal distribution of amplitude and FWHM, obtained from the MCMC fitting using the `emcee` sampler. This figure is plotted using `corner.py` (Foreman-Mackey 2016).

closely mimic the properties observed in intrinsic flare data.

Besides simulation of flare events, we also generate a series of simulations of non-flare events to establish a contrasting group in the training set. To distinguish these events from flare, which exhibits an asymmetric profile characterized by a rapid rise and gradual decay, we employ a symmetric Gaussian profile parameterized by sigma and amplitude. The sigma values are derived from a log-normal distribution with parameters $\mu = 3$ and $\sigma = 1$, while the amplitude values are obtained by sampling a half-normal distribution with parameter $\sigma = 1$. Similar to the simulated flare events, the simulated non-flare events are added into noise following a standard normal distribution. Both types of simulated events have a 2-minute cadence, which is consistent with the TESS photometry we used here.

Before incorporating the simulated events into the training set, we perform additional steps to ensure their close resemblance to the preliminary flare candidates. In accordance with the criteria used for identifying preliminary flares in Section 3.4, we require the generated events to have a minimum of two consecutive epochs with flux values greater than 3. Subsequently, we extend these epochs using the previously described algorithm, which involves expanding the left and right sides of each

candidate event until one and two consecutive epochs, respectively, have flux values less than 1, and then truncating the left epochs. Moreover, for non-flare events with five or more epochs, we require that the peak epoch must be located on the right side of the event, thereby creating a clearer distinction between flare and non-flare events in the training set. A selection of events from the training set is illustrated in Figure 7.

We generate a total of 5,000 simulated events for flares and non-flares, separately. These events are subsequently partitioned into training, validation, and test sets following a 3:1:1 ratio. A visual representation of the amplitude v.s. duration distributions for the simulated flare and non-flare events within the training set is provided in Figure 8. These simulated flare events have a wider range of amplitude values that extend to considerably higher levels, and generally exhibit longer durations in comparison to non-flare events. These discrepancies in amplitude and duration are in accordance with the inherent properties of flares and non-flares. Flares typically manifest substantial brightness increases and last for extended durations, whereas non-flares, encompassing noise and artifacts, display less pronounced amplitude variations and shorter durations.

4.3. *Feature selection and extraction*

Feature extraction is essential in machine learning applications, as it converts time-series data with varying durations into structured vectors suitable for input into the classifier. Moreover, the careful selection of an appropriate and informative feature set is also crucial to ensure the critical information embedded within the data. The chosen features should effectively encapsulate the intrinsic characteristics of the events, allowing the classifier to distinguish more accurately between distinct categories and yield more reliable results.

In this study, we employ the Python package `tsfresh` (Christ et al. 2018) to facilitate feature selection and perform feature extraction. This package is designed for machine learning applications and is capable of automatically identifying and extracting relevant features from time-series data using hypothesis testing. We initially use `tsfresh` to select a comprehensive list of features, from which we subsequently handpick a set of valuable features that efficiently distinguish between flare and non-flare events. These selected features are presented in Table 2.

For the training of the RF classifier, we transform each simulated event into a single 9×1 vector, corresponding to the selected features. The feature extraction process not only vectorizes the events but also emphasizes the distinguishing characteristics that differentiate flare and non-flare events, enabling the classifier to focus on the most significant aspects of the data.

4.4. *Hyperparameter tuning and model training*

Following feature extraction, we proceed with hyperparameter tuning, a crucial step in optimizing the classifier's performance. This process involves determining the optimal combination of hyperparameters, which are selected based on their capacity to maximize the score of the RF model on the validation set.

We employ the Python package `optuna` (Akiba et al. 2019) to tune the following hyperparameters of the RF classifier within the specified ranges, considering a balance between model complexity and computational efficiency:

- `n_estimators`: The number of trees in the forest. Range: (100, 1000, step=100)
- `max_depth`: The maximum depth of the trees. Range: (3, 17, step=2)
- `max_features`: The number of features to consider when seeking the best split. Range: (2, 5, step=1)

The `GridSampler` in `optuna` is used to perform a grid search, training the RF classifier with all possible combinations of hyperparameters and evaluating their accuracy scores on the validation set. The following hyperparameters produce the highest accuracy score (0.993) on the validation set:

- `n_estimators`: 100
- `max_depth`: 7
- `max_features`: 2

We select the corresponding model as the final model. Its performance is assessed on the test set, yielding an F1 score of 0.994, which is calculated as the harmonic mean of precision and recall.

Moreover, we can extract the feature importance after the training process, which assigns an importance score to each feature based on its contribution to the decision-making process. The significance of our selected features is shown in Figure 9, which illustrates the relative contribution of each feature to the classification process, offering insights into their relevance in the context of flare identification. The `first_location_of_maximum` feature, capturing the relative location of peak flux, emerges as the most important, which is reasonable given that flares exhibit a rapid rise and gradual decay.

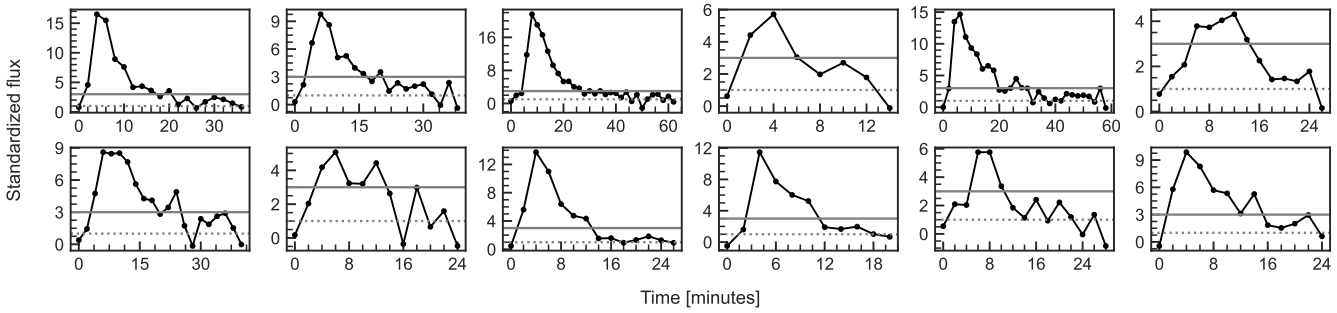

(a)

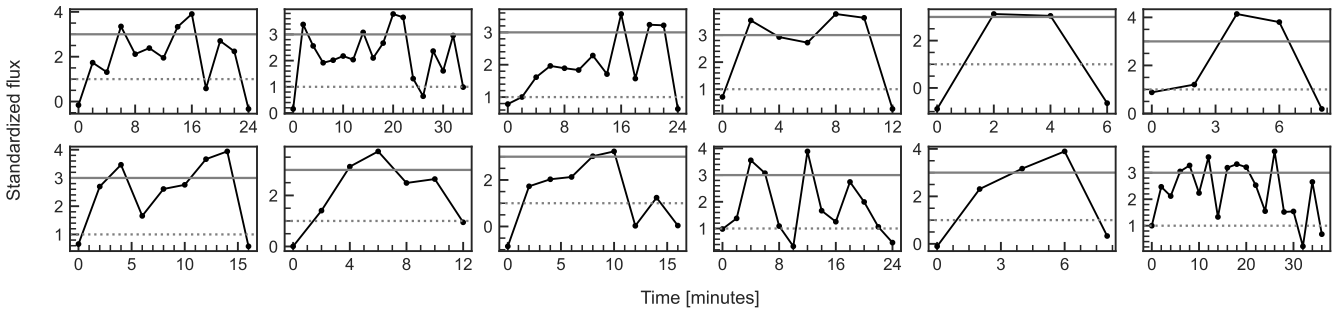

(b)

Figure 7. Examples of simulated events in the training set: (a) Flares, (b) Non-flares.

Table 2. All 9 Statistical Features Selected for Classification.

Feature	Description
abs_energy	Sum over the squared values of the time series
first_location_of_maximum	Relative location of the first maximum value in the time series
index_mass_quantile ($q = 0.5$)	Mass center of the time series
kurtosis	Kurtosis of the time series
length	Length of the time series
maximum	Highest value of the time series
root_mean_square	Root mean square of the time series
skewness	Sample skewness of the time series
standard_deviation	Standard deviation of the time series

NOTE—These features are computed using the Python package `tsfresh` (Christ et al. 2018). For details on these features and algorithms, see https://tsfresh.readthedocs.io/en/latest/text/list_of_features.html.

4.5. *Validating the preliminary flare candidates*

After training the RF classifier, we apply it to the preliminary flare candidates. As outlined in Section 4.3, we extract the corresponding set of features for these candidates. In cases where the candidates contain missing values, we employ a linear fitting method to interpolate them prior to feature extraction. The resulting feature vectors are then fed as input into the RF classifier.

The RF classifier computes a probability score for each candidate, indicative of its likelihood of being a intrinsic flare. We filter the preliminary flare candidates by applying a probability threshold of 0.5. Candidates with a probability score above this threshold are classified as validated flare events, while others are considered false

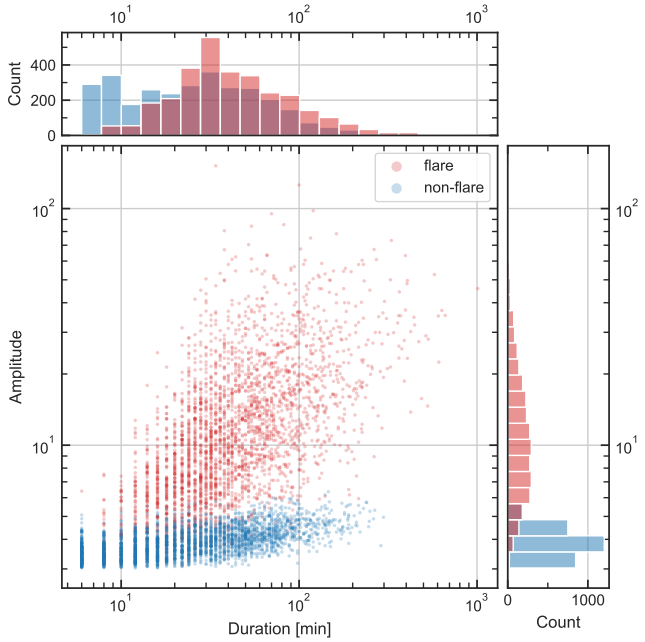

Figure 8. Joint distribution of amplitude and duration for the simulated flare events (red) and non-flare events (blue). The scatter plot in the central panel displays the relation between amplitude and duration for both classes. Marginal histograms along the top and right sides show the distributions of duration and amplitude separately. Both classes exhibit distinct distributions in terms of amplitude and duration, aiding in their differentiation during the analysis.

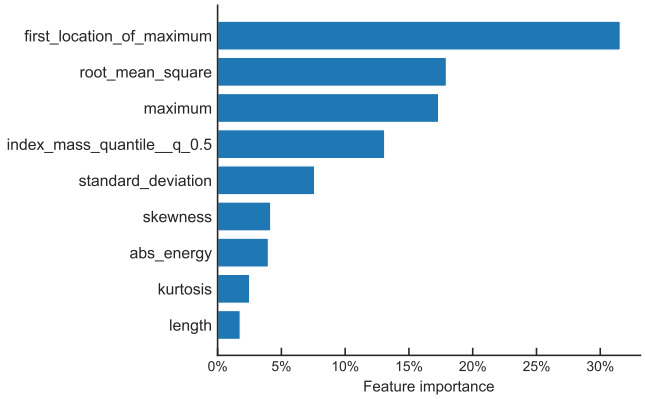

Figure 9. The importance of all 9 features in the training of the Random Forest classifier.

positives. This filtering effectively refines the flare candidate list, retaining only the events with a high probability of being intrinsic flares for further investigation.

To further improve the reliability and accuracy of the flare validation process, we perform an additional manual verification of the filtered flare candidates through visual inspection. During this process, we identify several common sources of false positives, including glitches in the light curves, unclassified CVs in the SIMBAD database, SSO encounters not captured in the SkyBoT query (potentially due to unknown SSOs or bright SSOs passing by without falling within the queried cone area), and low amplitude candidates exhibiting flare-like profiles but suffering from poor light curve quality.

5. RESULTS

From a total of 30 847 available 2-minute cadence light curves of 11 093 compact stars, we identified 5848 events as preliminary flare candidates. After excluding 486 events that are attributed by SSOs, we validated the remaining 5362 events with the help of our RF classifier, which flagged 2642 of these events as false positives. Finally, we confirmed 960 flare to be real events with further visual inspection of the remaining 2720 candidates. These confirmed flare events originated from 190 compact targets, which include 788 events from 131 white dwarfs and 172 events from 59 hot subdwarfs. Table 3 provides the observed properties of all confirmed flare events, such as peak time, amplitude and energy in TESS bandpass (see Section 5.2). Table 4 presents the key attributes of the flaring compact stars, including their classification, flare frequency and logarithm of fractional flare luminosity (see Section 5.3.1).

5.1. *Contamination check*

Prior to analyzing our results, it is vital to refine our sample of flaring compact stars to more accurately characterize the flare activity inherent to hot subdwarfs and white dwarfs. This refinement ensures the exclusion of targets where flare activities might potentially originate from contaminating sources other than the compact stars themselves, such as nearby objects or companion stars of the compact target.

5.1.1. *Evaluating pollution level*

Due to the relatively low angular resolution of TESS (21 arcsec pixel^{-1}), there is a considerable risk that the photometry may be contaminated by nearby objects. To address this concern, we developed an open-source script, `tpfi`, which generates identification charts for TESS target pixel files, as illustrated in Figure 10. Our script, based on `tpfplotter`[7] (Aller et al. 2020), introduces a notable feature: the ability to visualize the identical sky coverage of the target pixel file as provided

[7] https://github.com/jlillo/tpfplotter

Table 3. Catalog of All 960 Flares Observed Across 30 847 Compact Stars at 120 s Cadence during TESS Cycle 1-4.

TIC	Sector	$t_{\rm start}$ (BTJD)	$t_{\rm peak}$ (BTJD)	$t_{\rm stop}$ (BTJD)	SNR	A ($\Delta F/F$)	ED (s)	$E_{\rm TESS}$ (erg)
6997163	46	2576.0223	2576.0251	2576.0446	4.65	0.101	110(10)	$1.03(0.15)10^{35}$
20656977	20	1845.9203	1845.9230	1845.9439	13.17	0.577	415(24)	$1.53(0.09)10^{33}$
21860382	52	2719.4594	2719.4622	2719.4844	4.07	1.183	1098(100)	$1.05(0.10)10^{33}$
23226265	9	1546.4458	1546.4472	1546.4597	6.51	0.188	122(11)	$1.20(0.11)10^{32}$
23226265	9	1547.6653	1547.6694	1547.6750	3.69	0.106	54(9)	$5.37(0.85)10^{31}$
23226265	9	1559.3961	1559.4002	1559.4113	4.95	0.146	95(10)	$9.36(0.97)10^{31}$
23226265	9	1566.0406	1566.0600	1566.0892	10.76	0.318	538(20)	$5.30(0.20)10^{32}$
23226265	36	2283.5776	2283.5818	2283.5943	14.51	0.294	110(6)	$1.08(0.06)10^{32}$

NOTE— The table presents the details of the 960 flare events. Columns are TIC ID, Sector, start time, peak time, stop time, signal-to-noise ratio, amplitude, equivalent duration, energy in the TESS bandpass. The start, peak and stop time are in Barycentric TESS Julian Date (BTJD). The signal-to-noise ratio (SNR) is the maximum value in the standardized light curve during the flare event. Uncertainties are given in parentheses.
(This table is available in its entirety in machine-readable form.)

Table 4. Catalog of All 190 Flaring Compact Stars.

TIC	Spectral Type	Object Type	$L_{\rm TESS}$ (erg/s)	$N_{\rm flares}$	Flare freq. (Sector^{-1})	$\log(L_{\rm fl}/L_{\rm TESS})$	PL
6997163	sdB+F/G/K	HotSubdwarf	$9.37(1.06)10^{32}$	1	0.5	-4.54	0
20656977	DA+M	WhiteDwarf	$3.69(0.04)10^{30}$	1	1.0	-3.68	0
21860382	DA	WhiteDwarf	$9.54(0.07)10^{29}$	1	0.333	-3.60	2
23226265	cand-DAV	WhiteDwarf	$9.86(0.06)10^{29}$	6	3.0	-3.58	2
23385704	WD	WhiteDwarf Candidate	$1.23(0.01)10^{30}$	1	0.5	-4.00	2
23936802	WD	WhiteDwarf	$6.41(0.10)10^{30}$	1	0.25	-4.26	0
23992223	DA	WhiteDwarf	$6.20(0.05)10^{30}$	1	0.5	-4.78	1

NOTE—The table presents the details of the 190 flaring compact stars. Columns are TIC ID, spectral type given by the TASC WG8 target list, object type queried from the SIMBAD database, stellar luminosity in the TESS bandpass, number of observed flares, flare frequency per Sector, logarithm of the fractional flare luminosity, and pollution level of the target (see Section 5.1). The description of the object types is presented in https://simbad.cds.unistra.fr/guide/otypes.htx. Uncertainties are given in parentheses.
(This table is available in its entirety in machine-readable form.)

by the Digital Sky Survey (DSS)[8]. This enhancement allows for a more convenient assessment of the contamination level of a target. In addition to its applicability to TESS, we extended the use of `tpfi` to Kepler and K2 missions. We anticipate that this enhancement will make the script valuable to broader communities, for instance, the exoplanet and variable star research communities. Our script is publicly available on Github[9].

Following these considerations, we employed `tpfi` to create identification charts for all compact stars in our sample. We thus can conduct a visual examination of each of the 190 compact stars in our sample to assess the potential for contamination from nearby sources. In order to systematically quantify the contamination, we

[8] https://archive.eso.org/dss/dss

[9] https://github.com/keyuxing/tpfi

defined the pollution level (PL) for each star, as shown in Table 4. A PL of 0 indicates that the target is the only object within the aperture, with no other stars that could significantly impact the photometry present. A PL of 1 denotes that the target is the brightest object within the aperture, but there are other dim stars present. Lastly, a PL of 2 refers to the cases where the target is not the brightest object within the aperture or near a much brighter star. To illustrate, Figure 10(a) represents a scenario with a PL of 0, indicating an unpolluted target star. Figure 10(b) displays minor contamination, warranting a PL of 1. Cases of severe contamination, as demonstrated by Figures 10(c) and (d), are assigned with a PL of 2.

In our categorization, 60 stars have a PL of 0, 55 stars fall into the PL 1 category, and 75 stars are classified with a PL of 2, which corresponds to 371, 217 and 372 flares, respectively. These pollution levels offer a crude estimate of potential contamination. They are particularly useful in downstream analyses, where the potential impact of such contamination on our flare detection results must be considered. We also note that a high PL does not necessarily disqualify a star as a flare candidate. However, stars with a high PL warrant additional caution and follow-up investigation to confirm the source of the flare events.

5.1.2. *Selecting the refined sample*

By evaluating the pollution level for each flaring compact star in our sample, we effectively mitigate the influence of nearby objects. To further address potential contamination arising from companion stars, we cross-match the flaring compact stars with Gaia Data Release 3 (DR3; Gaia Collaboration et al. 2016, 2023) to acquire their stellar parameters, and established the following filtering criteria:

- Assigned a PL greater than 0
- Labelled as binary in WG8 target list
- Positioned within the main sequence of the Gaia Hertzsprung-Russell (H–R) diagram (see Figure 11; $G_{\rm BP} - G_{\rm RP} > 1$ and $G_{\rm abs} < 12$), or not provided with $G_{\rm BP} - G_{\rm RP}$ or $G_{\rm abs}$ in Gaia DR3
- Listed in Schaffenroth et al. (2022), which performed a comprehensive search of the light curves of hot subdwarfs in TESS Sector 1-36 for binary effects, such as the reflection effect and ellipsoidal deformation

Any star from our sample meeting these criteria is excluded. This procedure ensures that we concurrently eliminate contamination from nearby objects and companion stars.

Through the application of these criteria, we produce a more accurate and representative sample of flaring compact stars, consisting of 13 hot subdwarfs and 11 white dwarfs. The parameters of the flaring compact stars within our refined sample are listed in Table 5.

5.2. *Flare properties*

For each identified flare event, we measured properties such as duration, amplitude, equivalent duration, and energy in the TESS bandpass. Figure 12(a) displays the properties of all 960 confirmed flare events, whereas Figure 12(b) illustrates those from the refined sample.

5.2.1. *Amplitude*

The flare amplitude, defined as the maximum increase in flux during the flare event relative to the flux of the star in its quiescent state, is calculated as:

$$A = \frac{F_{\rm peak} - F_{\rm quiescent}}{F_{\rm quiescent}}, \tag{3}$$

where A represents the flare amplitude, $F_{\rm peak}$ is the maximum flux observed during the flare event and $F_{\rm quiescent}$ is the quiescent flux.

5.2.2. *Equivalent Duration*

The equivalent duration (ED; Gershberg 1972) provides an estimate of the energy output of a flare relative to the quiescent emission of the star. Expressed in units of time (e.g., seconds), the ED represents the duration for which the star would need to emit at its quiescent brightness level to equal the excess energy released by the flare. It is calculated as follows,

$$\mathrm{ED} = \int \frac{F_{\rm flare}(t) - F_{\rm quiescent}}{F_{\rm quiescent}} \mathrm{d}t, \tag{4}$$

where the integral is computed by a trapezoidal sum of the light curve between the start and stop times of the flare. The uncertainty of ED is calculated following Davenport (2016).

5.2.3. *Energy*

Typically, the total energy emitted by a stellar flare (i.e., the bolometric flare energy) can be estimated if the effective temperature and radius of the star are known (see, e.g., Shibayama et al. 2013; Günther et al. 2020). However, the result of the cross-matching of the flaring compact stars with Gaia DR3 shows that only a small

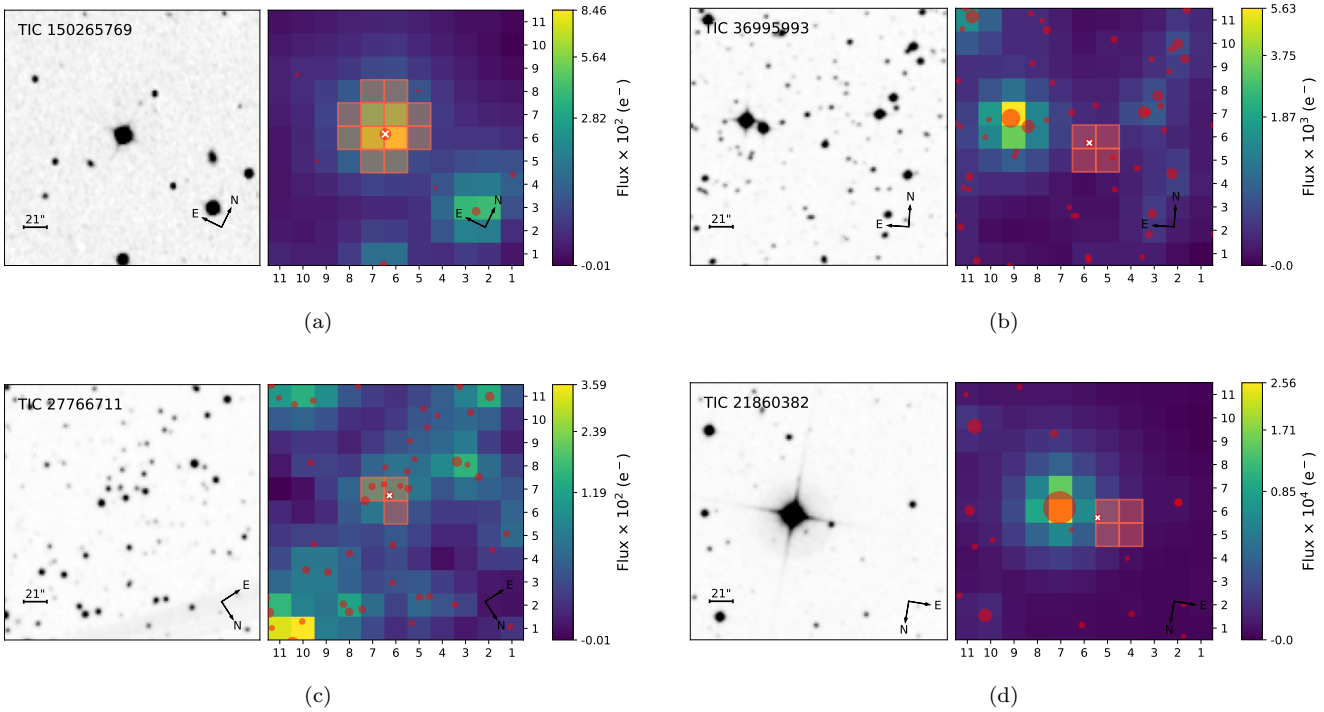

Figure 10. Examples of the identification charts provided by `tpfi`: (a) an ideal situation that the aperture only hosts the target with no other bright stars nearby, (b) the aperture hosting the target star and another dimmer star, (c) the aperture hosting numerous stars with comparable brightness alongside the target, (d) only the target resides within the aperture, but in proximity to a bright star. In each chart, the right panel overlays the Gaia DR3 catalog onto the target pixel file, with the target denoted by a white cross symbol. The size of the circle represents the relative brightness of the stars, as indicated by the Gaia G magnitude. The red region indicates the default aperture mask used by SPOC for photometry extraction. The left panel shows the same sky coverage, using DSS2 red images, with the same orientation.

subset (∼10%) of our samples have these stellar parameters available, which restricts our ability to calculate the bolometric flare energy across the entire sample.

Given these limitations, we refocused towards estimating the flare energy in the TESS bandpass, a measure that provides insight into the observable energy released during the flare event. It is important to note that the energy estimated in the TESS bandpass can be significantly smaller than the bolometric flare energy. This discrepancy arises because flares, often approximated by a 9000 K blackbody (Jackman et al. 2022), primarily emit energy in the high-energy range at short wavelengths, which fall outside the TESS bandpass.

We first calculate the luminosity of the star in the TESS bandpass using the following formula:

$$L_{\rm TESS} = 4\pi d^2 \times F_{\rm TESS}, \tag{5}$$

where d is the distance to the star derived from its parallax listed in Gaia DR3. The flux of the star in the TESS bandpass $F_{\rm TESS}$ is calculated via the following relation:

$$F_{\rm TESS} = 10^{-0.4T} \times F_0, \tag{6}$$

where T is the TESS magnitude derived from the TESS Input Catalog version 8.2 (TIC v8.2; Stassun et al. 2019; Paegert et al. 2021) and $F_0 = 4.03 \times 10^{-6}$erg s^{-1} cm^{-2}, which is the flux corresponding to $T = 0$ (Sullivan et al. 2015). The uncertainty in the calculated luminosity $L_{\rm TESS}$ accounts for uncertainties in both the TESS magnitude and the parallax.

Lastly, we compute the flare energy in the TESS bandpass by:

$$E_{\rm TESS} = {\rm ED} \times L_{\rm TESS}, \tag{7}$$

where ED is the equivalent duration of the flare and $L_{\rm TESS}$ is the calculated luminosity of the star in the TESS bandpass.

For six of the flaring compact stars, which correspond to 120 flare events, the parallax parameters were not available in Gaia DR3. As a result, we were only able to calculate the energies for the remaining 846 flares. The median value of uncertainties associated with $E_{\rm TESS}$ is 22.6%.

5.3. *Flare activities*

We here investigate the flare activity exhibited by compact stars. We compute the fractional flare lumi-

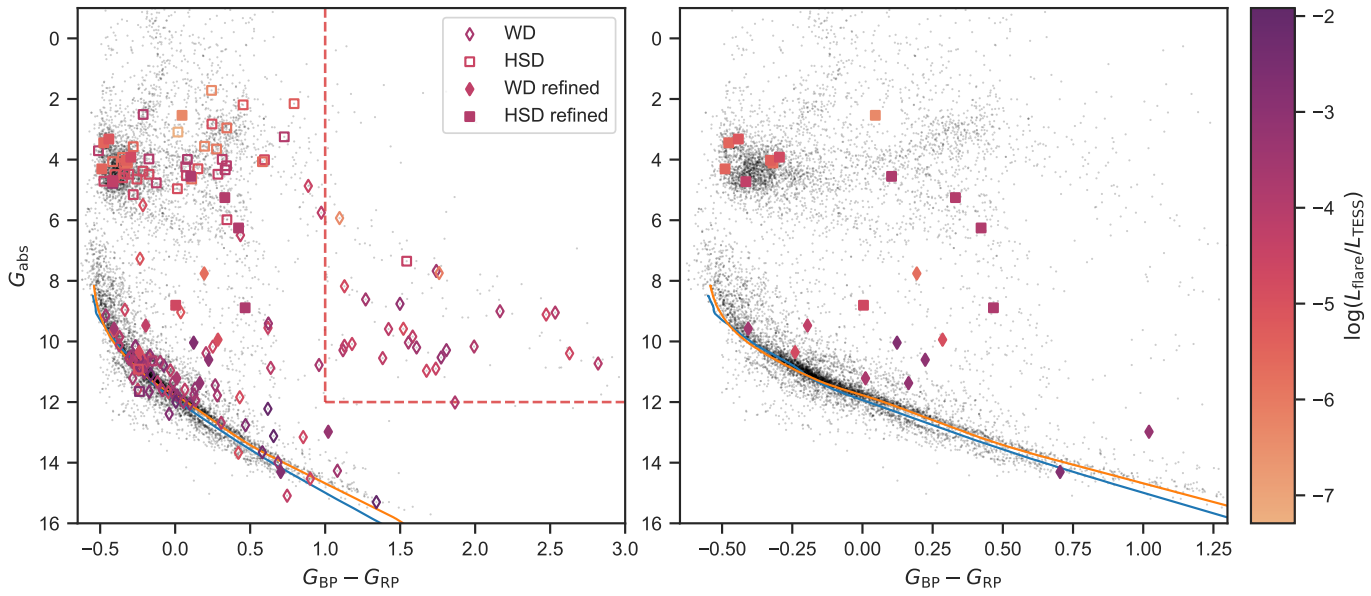

Figure 11. Gaia H–R diagram of the flaring compact stars included in our study. The x-axis is the BP-RP color index, while the y-axis is the absolute Gaia G magnitude, both derived from Gaia DR3. The color of each data point correlates with the $\log(L_{\rm flare}/L_{\rm TESS})$ for each star. Black dots represent all compact stars in the WG8 target list. White dwarfs are denoted with diamond markers, while hot subdwarfs are signified by square markers. Filled markers represent the stars from our refined sample, while open markers denote the others. The left panel contains all flaring compact stars in our result, while the right panel zooms in on the refined sample. The red dashed lines in the left panel indicate the threshold set in the third criterion for selecting the refined sample (Section 5.1.2). The orange and blue lines are the cooling tracks for DA and DB WDs separately, each with a mass of 0.61 $M_\odot$ and metallicity $Z = 0.04$, obtained from `BaSTI` (Salaris et al. 2021).

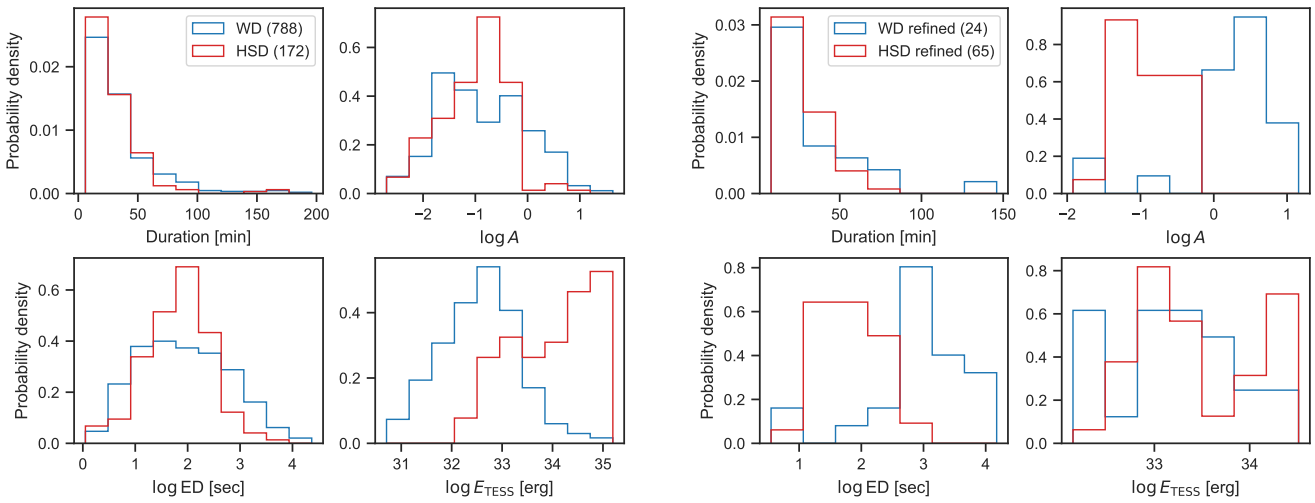

Figure 12. Distributions of the properties of: (a) all the confirmed flare events, (b) the flare events originated from the refined sample (Section 5.1.2). The blue lines represent the flare events originated from white dwarfs, while the red lines represent the flare events originated from hot subdwarfs. The numbers within the parentheses indicate the count of flare events in specific subsets. The properties are: duration, logarithm of amplitude, logarithm of equivalent duration and logarithm of energy in the TESS bandpass.

Table 5. Catalog of Flaring Compact Stars in the Refined Sample.

TIC	Gaia DR3 Source ID	Spectral Type	T (mag)	$G_{\rm BP} - G_{\rm RP}$ (mag)	$G_{\rm abs}$ (mag)	$N_{\rm flares}$	Flare freq. (Sector^{-1})	$\log(L_{\rm fl}/L_{\rm TESS})$
24620431	5631444059185050240	cand-sd_var	14.2923	0.3311	5.254	3	3.0	-3.97
118327563	5000760581717433088	sdB	10.515	-0.319	4.1129	1	0.5	-5.68
121318590	3073231760953563264	He-sdO	11.631	-0.4763	3.4455	1	0.5	-5.5
150265769	781164326766404736	sdO	11.5152	-0.4893	4.305	1	0.5	-5.47
157332788	1584606197921640448	sdO	12.6414	-0.442	3.3212	2	0.4	-5.14
167976324	5465148904077059968	sdO	12.779	-0.3275	4.0243	1	0.333	-5.35
219974863	6468929937072637312	sdOB	12.4	-0.2958	3.9193	1	0.5	-4.69
234281664	6404530097924835968	sdB	12.901	0.1036	4.5531	4	1.333	-3.81
262921847	4673757096243879168	sd	13.19	0.4665	8.8891	32	3.556	-3.83
294728980	5228352822889323776	sdBVg	15.0446	0.0036	8.805	1	0.25	-4.65
349408306	5282634371914454912	cand-sd_var	15.8445	0.4225	6.2553	15	1.154	-3.87
369965957	4900121354714539136	sdO	9.282	0.0458	2.5392	2	0.667	-6.34
455275325	3848227342153889280	sdBV	15.891	-0.4153	4.7263	1	0.333	-4.27
23936802	2095603539740855296	WD	16.108	-0.1957	9.4744	1	0.25	-4.26
229742116	2265642978613763072	WD	16.9899	0.1643	11.3747	7	0.333	-3.12
253039181	830644063706298496	DA	14.2512	0.2853	9.9416	1	0.5	-4.93
269750545	3422762075019208576	WD	17.2706	0.0108	11.2162	1	0.333	-3.74
272613022	1291066348840336128	WD	16.7045	0.2235	10.6042	3	1.0	-3.05
344926886	3834915417437497088	WD	16.9825	1.0206	12.9796	1	0.5	-3.24
422947065	2503828498910129664	DA	12.1658	0.1935	7.7575	2	0.5	-5.71
719967315	3403722102745482112	WD	17.1056	0.7038	14.3053	4	1.333	-2.75
740573368	872136162206017792	WD	17.8418	-0.4069	9.5778	1	0.333	-3.54
778284326	5608058473357824128	cand-DxV	16.0935	0.1232	10.0411	2	1.0	-2.71
1717585166	2143573131817151616	WD	16.8634	-0.2401	10.3545	1	0.091	-4.75

NOTE—This table lists the 13 hot subdwarfs and 11 white dwarfs in our refined sample. Columns are TIC ID, Gaia DR3 source ID, spectral type given by the TASC WG8 target list, TESS magnitude from TIC v8.2, BP-RP color index from Gaia DR3, absolute Gaia G magnitude from Gaia DR3, number of observed flares, flare frequency per Sector and logarithm of the fractional flare luminosity.

nosity for each of these 190 stars to quantitatively measure their strength of flare activity. Following this, these stars are positioned onto the H–R diagram. We also calculate the flare frequency distribution (FFD) and the fit its power law index for different subsets of samples.

5.3.1. *Fractional flare luminosity*

For each flaring compact star, we calculate the fractional flare luminosity, represented as $L_{\rm flare}/L_{\rm TESS}$, which is the total luminosity emitted by flares relative to the total luminosity emitted by the star through the TESS bandpass. Serving as an intuitive metric, it quantifies the intensity of stellar flare activity. The metric was originally denoted as $L_{\rm fl}/L_{\rm Kp}$ in Lurie et al. (2015) for characterizing the flare activity level of the flaring stars with Kepler photometry. This metric is now widely used in various flare research (see, e.g., Davenport 2016; Davenport et al. 2019). In certain cases, the $L_{\rm Kp}$ has been substituted with the bolometric luminosity $L_{\rm bol}$ (see, e.g., Yang & Liu 2019; Ilin et al. 2021).

We calculate this ratio for a star using the following equation,

$$\frac{L_{\rm flare}}{L_{\rm TESS}} = \frac{\sum {\rm ED}_i}{t_{\rm obs}}, \tag{8}$$

where ${\rm ED}_i$ represents the ED of each flare for the star, and $t_{\rm obs}$ is the total observation time for the star by TESS. A higher value of this ratio signifies enhanced flare activity, indicative of an increased level of stellar magnetic activity.

Our calculation results are graphically presented by locating the flaring compact stars on the H–R diagram in Figure 11, using $G_{\rm BP} - G_{\rm RP}$ and $G_{\rm abs}$ obtained from Gaia DR3. We distinguish between hot subdwarfs and white dwarfs in the diagram and specifically illustrate the fractional flare luminosity across the flaring compact stars in our refined sample.

5.3.2. *Flare frequency distribution*

The Flare Frequency Distribution (FFD) represents the frequency of flare occurrences as a function of their energy. Typically described by a power law (Lacy et al. 1976), the FFD can be expressed as,

$$\mathrm{d}N(E) = kE^{-\alpha}\mathrm{d}E, \tag{9}$$

where N represents the number of flares occurring within a specific observation duration, E denotes the flare energy, k is a proportionality constant, and α is the power-law index (Jackman et al. 2021). This power-law index, α, plays a critical role in investigating flare production mechanisms, and its derivation is essential to our study of flare activities in compact stars.

Table 6. Power-law Fit Results to Cumulative FFDs.

Type	α^*	β	$N_{\rm fit}{}^\dagger$
WD	2.04 ± 0.13	$34.77^{+4.36}_{-4.36}$	184
WD refined	1.73 ± 0.20	$23.39^{+6.60}_{-6.59}$	16
HSD	1.98 ± 0.18	$33.96^{+6.49}_{-6.49}$	51
HSD refined	1.77 ± 0.19	$26.44^{+6.41}_{-6.44}$	29

* The slope of the cumulative FFD is $1 - \alpha$.

† The number of flares used for fitting.

Due to differences in observation durations for various flaring compact stars, a direct computation of their FFD is not feasible. We hence employ the cumulative FFD to estimate α instead. The cumulative FFD is derived by integrating Equation (9), leading to

$$\log(\nu) = \beta + (1-\alpha)\log(E), \tag{10}$$

where $\beta = \log(\frac{k}{1-\alpha})$, and ν denotes the frequency of flares, i.e. the number of flares per unit time with energy exceeding a specific threshold.

We compute four distinct cumulative FFDs, each representing flare events from all observed hot subdwarfs, white dwarfs, and their respective subsets from our refined sample (see Section 5.3.1). For every flare event with energy E, we calculate the corresponding ν as follows:

$$\nu = \sum \frac{N_i(>E)}{t_i}, \tag{11}$$

where $N_i(>E)$ is the number of flares with energies greater than E and t_i is the observation time for each flaring compact star.

Subsequently, we use the MCMC method to fit a linear regression model to each cumulative FFD. This approach effectively mitigates binning effects, providing an advantage over the conventional method of histogram generation and straight-line fitting (Maschberger & Kroupa 2009). We only fit the portion of the cumulative FFDs where we consider our sample to be complete. Figure 13 displays the cumulative FFDs with the corresponding best-fit lines, while Table 6 lists the fitted values for α and β, and the number of flares used for the fitting.

6. SUMMARY AND DISCUSSION

Based on the 1-4 cycles of TESS photometry, we comprehensively investigated the flaring activity observed in HSDs and WDs, which identified 960 flare events from 190 compact stars (Table 3 & 4). We pioneered

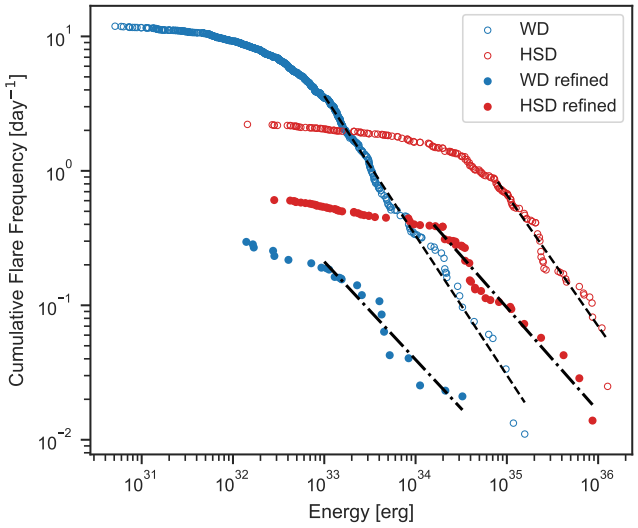

Figure 13. Cumulative FFDs and respective power law fits. The blue and red open circle markers represent flares from all hot subdwarfs and white dwarfs, respectively. The filled circle markers of the same color signify flares from the hot subdwarfs and white dwarfs in our refined sample. The dashed and dash-dot black lines represent the best-fit power laws to the cumulative FFDs of the full and refined sample, respectively.

a new method for flare detection, specifically designed to address short-term periodic variations in light curves. This method enhances flare detection capabilities when applied to the light curves, despite the complexities introduced by common phenomena in compact stars such as pulsation and binary effect. We also considered potential interferences from CVs and SSOs and eliminated them. In addition, we implemented a validation step using machine learning to effectively filter out false positives. These rigorous detection and validation processes assured the reliability of the detected flares, enabling us to establish the first flare catalog of compact stars, which contains 131 WDs and 59 HSDs with 788 and 172 flare events, respectively.

However, as the pixel size of TESS covers 21 arcsecs, the flaring targets, relatively faint in brightness, have a high chance to be polluted by their nearby counterparts. In addition, those targets may be in binary systems whose companion will also affect the statistical properties of flares in those compact stars. Therefore, to obtain a clean flare catalog that accurately represents the behavior of flaring compact stars, we developed an open-source script, `tpfi`. This script facilitates the generation of identification charts for TESS target pixel files, thereby enabling a detailed visual inspection for potential contamination sources near the target. Moreover, we strived to exclude flare events from main-sequence companion stars using strict selection criteria based on Gaia DR3. These steps are crucial for maintaining the reliability of our results and the subsequent analysis. We finally selected a refined sample consisting of 13 HSDs and 11 WDs, which correspond respectively to 65 and 24 flare events (Table 5).

A glimpse is paid on the location of those two different samples on the HR diagram (Figure 11). Compared to the entire sample, the refined one indeed has a much closer location to where the compact stars should be. We recall that, to our knowledge, there is no dedicated survey searching for flare events in compact stars due to a few reasons, for instance, the complexity to detrend light curves (Pietras et al. 2022). Our catalog could be the first step to such research, definitely, triggering new interests in stellar activity in highly evolved compact stars. In the refined sample, four or five WDs could be good candidates for future inspection, for instance, to ascertain whether they are single stars or in binary system. There are seven stars in the color cluster of HSD range but needed particular attention to binary information in future inspection since more than half HSD stars reside in binary system (Schaffenroth et al. 2023). If confirmed, these candidates would be the first compact stars to exhibit a flare event. However, despite the above flaws in identifying the intrinsic flares in those stars, the properties of our two kinds of flare catalogs deserve further detailed discussion.

In our analysis of flare properties, contrasting observations emerged between the complete sample and the refined sample (Figure 12). For the complete sample, there was no discernible difference in the distributions of duration, amplitude, and ED between HSDs and WDs in general. Whereas the energy associated with the flare events in HSDs was found to surpass that from WDs by approximately an order of magnitude, due to the fact that the luminosity of HSD is much brighter than that of WD stars (Eqn. 7). We note that a large fraction of our entire sample is polluted by their nearby surroundings. The contaminating flares from nearby stars could jeopardize their intrinsic properties because the energy is calculated based on the luminosity and the detection ability is determined by the photometric precision. In addition, about one sixth of our targets are found in binary systems. This energy distinction could be attributed to their evolutionary difference: WDs are generally older than HSDs, implying that the companion stars of WDs, being older as well, exhibit reduced flare activity, as corroborated by Davenport et al. (2019).

Shifting the focus to the refined sample, the flare durations between HSDs and WDs displayed little variation. However, the amplitude and ED of flares from

WDs markedly exceeded those of HSDs. The mechanism of this difference is yet to be revealed if we assume that flares detected in the refined sample are completely from compact stars. As flare activity is highly related to the magnetic field, we here propose some preliminary explanations for the observational difference in the refined sample. Compared to WDs, HSDs have relatively weaker flaring levels, which might be related to magnetic strength. To current knowledge, magnetism in HSDs is very rare (Landstreet et al. 2012) and only a few HSD objects were claimed to have detectable magnetic field (Vos et al. 2021; Pelisoli et al. 2022). Nevertheless, the existence of magnetic field of WDs was expected (Blackett 1947) after the first detection of the magnetic field of A-type stars (Babcock 1947). Now that WDs are found with magnetism whose strength is in a large range from a few kG up to 1000 MG (e.g., Landstreet & Bagnulo 2019). Their magnetism is explained by fossil mechanisms or the conservation of magnetic flux (Woltjer 1964). Yet, a parity in energy distributions was observed, likely attributed to the higher luminosity of HSDs in comparison to WDs.

When we proceeded to analyze the FFDs, a notable observation emerged related to the power-law index α. We found that the FFDs from both HSDs and WDs have an index $\alpha \sim 2$ when fitted with the entire flare sample, while the FFDs have an index $\alpha \sim 1.75$ when fitted with the refined sample (see Figure 13 and Table 6). This divergence arises because the entire sample is polluted by flares originated from other cool main-sequence (MS) stars (F-M type stars). These stars, with FFDs having an index $\alpha \sim 2$ (e.g., Althukair & Tsiklauri 2023), significantly skew the index α when fitted with the entire sample, thus making it slightly larger. However, once the flare events from these MS stars are removed, we get FFDs that are less steep, which indicate a higher proportion of high energy flare events.

Before delving into potential mechanisms for flare occurrences on compact stars, it is pertinent to note that several studies have investigated stellar flares across spectral types A to M. They found that the FFD from A-type stars has an index $1 < \alpha < 1.5$ when using Kepler photometry, a finding that markedly deviates from the $\alpha \sim 2$ observed in cooler F-M type stars (Švanda & Karlický 2016; Yang & Liu 2019; Bai & Esamdin 2020; Althukair & Tsiklauri 2023). Yang et al. (2023) also reported $\alpha = 1.76 \pm 0.19$ for A-type stars based on TESS data. Although this value is higher than that obtained via Kepler photometry—likely due to increased contamination from lower angular resolution of TESS—it remains lower than indices for cooler MS stars. Such deviations in α have been interpreted as indicative of differing flare mechanisms between B/A type and cool MS stars.

This observation prompts us to compare HSDs with B/A-type MS stars, especially given the observed deviation in α between the FFDs derived from our entire and refined samples. Notably, both HSDs and B/A-type stars possess a radiative envelope, distinguishing them from cooler MS stars with convective envelopes. Despite the general expectation that these stars lack strong magnetic fields and are unlikely to produce flares through known dynamo mechanisms, as a result of the absence of a deep convective envelope (Charbonneau 2010), previous literature has reported that they might do show magnetic activities. For instance, Balona (2021) reported flare events on B/A-type stars and argued that observed rotational modulation in flaring B/A-stars suggests strong surface magnetic fields. Similarly, Momany et al. (2020) attributed the periodic first mode of variability in EHB stars (sdB stars in globular clusters) to magnetic spots and reported a superflare event in an apparently single sdB star, TIC118327563, also identified in our study and listed in Table 5.

We thus hypothesize that flares on HSDs may share an underlying mechanism with those observed in early-type stars, contingent upon the flares in our refined sample originated exclusively from compact stars. However, the nature of the magnetic fields responsible for spots and flares on B/A-type stars remains unclear. Švanda & Karlický (2016) assumed that these magnetic fields could be amplified by dynamo processes in the convective cores of A-type stars, subsequently becoming unstable and rising as magnetic ropes through the radiative envelope. Balona (2019) also suggested that differential rotation might suffice to generate local magnetic fields in B/A-type stars, presenting an exciting direction for future research to deepen our understanding of magnetic activities in stars with radiative envelopes. It is crucial to emphasize, however, that this hypothesis is preliminary and warrants further in-depth investigation.

Although our results indicate a similar decrease in index α for WDs, the limited sample size for fitting this α necessitates further validation. Recent observations have shown the presence of spots on an increasing number of WDs (e.g., Kilic et al. 2015; Hoard et al. 2018; Hermes et al. 2021), implying that flares may indeed occur on these stars, as both phenomena are closely tied to magnetic fields. Moreover, spot modulation is empirically not restricted to purely convective or strongly magnetic WDs (Hermes et al. 2017), thereby opening the possibility for flare occurrences on WDs having a radiative envelope or relatively weak magnetic field. Additionally, the abrupt brightness variation of outbursts

is reported in WDs but with a different profile and duration compared to flares (e.g., Bell et al. 2016; Scaringi et al. 2022). We recall that there is no report of a flare event on WDs in any previous literature.

We finally propose some prospects for our discoveries of flare events in HSDs and WDs. Our methods are readily adaptable for similar analyses of the Kepler and K2 photometry, which boast a higher angular resolution of roughly 4 arcsec pixel^{-1}, reducing contamination from nearby objects significantly. Moreover, ground-based photometry is urgently required for our refined samples to confirm the flares from the compact stars unambiguously. We anticipate the ongoing photometry from the second extension mission of TESS, which will further enable continuous monitoring of flare events in the entire sample. In addition, our method and pipeline can be helpful for flare hunting in other types of stars, with high confidence and feasibility. Furthermore, our tool, `tpfi`, is well-integrated with Kepler/K2 photometry, which enhances contamination reduction. Beyond the research on stellar flares, the identification charts generated by `tpfi` can also be invaluable for other studies, for instance, exoplanet detection and variable star research, underscoring its broader astronomical applicability.

We acknowledge the support from the National Natural Science Foundation of China (NSFC) through grants 12273002, 11833002, 12090040, 12090042, 11988101 and 11933004. This work is supported by the science research grants from the China Manned Space Project. S.C. is supported by the Agence Nationale de la Recherche (ANR, France) under grant ANR-17-CE31-0018, funding the INSIDE project, and financial support from the Centre National d'Études Spatiales (CNES, France). The authors gratefully acknowledge the TESS team and all who have contributed to making this mission possible. Funding for the TESS mission is provided by the NASA Explorer Program.

REFERENCES

Akiba, T., Sano, S., Yanase, T., Ohta, T., & Koyama, M. 2019, in Proceedings of the 25th ACM SIGKDD International Conference on Knowledge Discovery and Data Mining

Aller, A., Lillo-Box, J., Jones, D., Miranda, L. F., & Barceló Forteza, S. 2020, A&A, 635, A128, doi: 10.1051/0004-6361/201937118

Althukair, A. K., & Tsiklauri, D. 2023, Research in Astronomy and Astrophysics, 23, 085017, doi: 10.1088/1674-4527/acdc09

Babcock, H. W. 1947, ApJ, 105, 105, doi: 10.1086/144887

Bagnulo, S., & Landstreet, J. D. 2021, Monthly Notices of the Royal Astronomical Society, 507, 5902, doi: 10.1093/mnras/stab2046

Bai, J.-Y., & Esamdin, A. 2020, The Astrophysical Journal, 905, 110, doi: 10.3847/1538-4357/abc479

Balona, L. A. 2019, Monthly Notices of the Royal Astronomical Society, 490, 2112, doi: 10.1093/mnras/stz2808

—. 2021, Frontiers in Astronomy and Space Sciences, 8, doi: 10.3389/fspas.2021.580907

Baran, A. S., Van Grootel, V., Østensen, R. H., et al. 2023, A&A, 669, A48, doi: 10.1051/0004-6361/202244888

Bastian, T. S., Dulk, G. A., & Slee, O. B. 1988, AJ, 95, 794, doi: 10.1086/114678

Bell, K. J., Hermes, J. J., Montgomery, M. H., et al. 2016, The Astrophysical Journal, 829, 82, doi: 10.3847/0004-637X/829/2/82

Benz, A. O., & Güdel, M. 2010, Annual Review of Astronomy and Astrophysics, 48, 241, doi: 10.1146/annurev-astro-082708-101757

Berthier, J., Carry, B., Vachier, F., Eggl, S., & Santerne, A. 2016, Monthly Notices of the Royal Astronomical Society, 458, 3394, doi: 10.1093/mnras/stw492

Berthier, J., Vachier, F., Thuillot, W., et al. 2006, in Astronomical Society of the Pacific Conference Series, Vol. 351, Astronomical Data Analysis Software and Systems XV, ed. C. Gabriel, C. Arviset, D. Ponz, & S. Enrique, 367–+

Blackett, P. M. S. 1947, Nature, 159, 658, doi: 10.1038/159658a0

Bognár, Z., Kawaler, S. D., Bell, K. J., et al. 2020, A&A, 638, A82, doi: 10.1051/0004-6361/202037470

Breiman, L. 1996, Machine Learning, 24, 123, doi: 10.1007/BF00058655

—. 2001, Machine Learning, 45, 5, doi: 10.1023/A:1010933404324

Brink, H., Richards, J. W., Poznanski, D., et al. 2013, Monthly Notices of the Royal Astronomical Society, 435, 1047, doi: 10.1093/mnras/stt1306

Bruch, A. 2022, Monthly Notices of the Royal Astronomical Society, 514, 4718, doi: 10.1093/mnras/stac1650

Charbonneau, P. 2010, Living Reviews in Solar Physics, 7, 3, doi: 10.12942/lrsp-2010-3

Charpinet, S., Brassard, P., Fontaine, G., et al. 2019, A&A, 632, A90, doi: 10.1051/0004-6361/201935395

Christ, M., Braun, N., Neuffer, J., & Kempa-Liehr, A. W. 2018, Neurocomputing, 307, 72, doi: https://doi.org/10.1016/j.neucom.2018.03.067

Culpan, R., Geier, S., Reindl, N., et al. 2022, A&A, 662, A40, doi: 10.1051/0004-6361/202243337

Davenport, J. R. A. 2016, The Astrophysical Journal, 829, 23, doi: 10.3847/0004-637x/829/1/23

Davenport, J. R. A., Covey, K. R., Clarke, R. W., et al. 2019, The Astrophysical Journal, 871, 241, doi: 10.3847/1538-4357/aafb76

Davenport, J. R. A., Hawley, S. L., Hebb, L., et al. 2014, The Astrophysical Journal, 797, 122, doi: 10.1088/0004-637x/797/2/122

Doorsselaere, T. V., Shariati, H., & Debosscher, J. 2017, The Astrophysical Journal Supplement Series, 232, 26, doi: 10.3847/1538-4365/aa8f9a

Feinstein, A. D., Montet, B. T., Ansdell, M., et al. 2020, The Astronomical Journal, 160, 219, doi: 10.3847/1538-3881/abac0a

Foreman-Mackey, D. 2016, The Journal of Open Source Software, 1, 24, doi: 10.21105/joss.00024

Foreman-Mackey, D., Hogg, D. W., Lang, D., & Goodman, J. 2013, Publications of the Astronomical Society of the Pacific, 125, 306, doi: 10.1086/670067

Gaia Collaboration, Prusti, T., de Bruijne, J. H. J., et al. 2016, A&A, 595, A1, doi: 10.1051/0004-6361/201629272

Gaia Collaboration, Vallenari, A., Brown, A. G. A., et al. 2023, A&A, 674, A1, doi: 10.1051/0004-6361/202243940

Gentile Fusillo, N. P., Tremblay, P. E., Cukanovaite, E., et al. 2021, Monthly Notices of the Royal Astronomical Society, 508, 3877, doi: 10.1093/mnras/stab2672

Gershberg, R. E. 1972, Astrophysics and Space Science, 19, 75, doi: 10.1007/BF00643168

Giorgini, J. D., Chodas, P. W., & Yeomans, D. K. 2001, in AAS/Division for Planetary Sciences Meeting Abstracts, Vol. 33, AAS/Division for Planetary Sciences Meeting Abstracts #33, 58.13

Godines, D., Bachelet, E., Narayan, G., & Street, R. 2019, Astronomy and Computing, 28, 100298, doi: https://doi.org/10.1016/j.ascom.2019.100298

Günther, M. N., Zhan, Z., Seager, S., et al. 2020, The Astronomical Journal, 159, 60, doi: 10.3847/1538-3881/ab5d3a

Heber, U. 2009, Annual Review of Astronomy and Astrophysics, 47, 211, doi: 10.1146/annurev-astro-082708-101836

Hermes, J. J., Gänsicke, B. T., Gentile Fusillo, N. P., et al. 2017, Monthly Notices of the Royal Astronomical Society, 468, 1946, doi: 10.1093/mnras/stx567

Hermes, J. J., Putterman, O., Hollands, M. A., et al. 2021, The Astrophysical Journal Letters, 914, L3, doi: 10.3847/2041-8213/ac00a8

Hippke, M., David, T. J., Mulders, G. D., & Heller, R. 2019, The Astronomical Journal, 158, 143, doi: 10.3847/1538-3881/ab3984

Hoard, D. W., Howell, S. B., Roettenbacher, R. M., et al. 2018, The Astronomical Journal, 156, 119, doi: 10.3847/1538-3881/aad238

Howard, W. S., & MacGregor, M. A. 2022, The Astrophysical Journal, 926, 204, doi: 10.3847/1538-4357/ac426e

Howell, S. B., Sobeck, C., Haas, M., et al. 2014, Publications of the Astronomical Society of the Pacific, 126, 398, doi: 10.1086/676406

Huber, P. J., & Ronchetti, E. M. 1981, New York, 1

Ilin, E., & Poppenhaeger, K. 2022, Monthly Notices of the Royal Astronomical Society, 513, 4579, doi: 10.1093/mnras/stac1232

Ilin, E., Schmidt, S. J., Poppenhäger, K., et al. 2021, A&A, 645, A42, doi: 10.1051/0004-6361/202039198

Jackman, J. A. G., Shkolnik, E. L., Million, C., et al. 2022, Monthly Notices of the Royal Astronomical Society, 519, 3564, doi: 10.1093/mnras/stac3135

Jackman, J. A. G., Wheatley, P. J., Acton, J. S., et al. 2021, Monthly Notices of the Royal Astronomical Society, 504, 3246, doi: 10.1093/mnras/stab979

Jenkins, J. M., Twicken, J. D., McCauliff, S., et al. 2016, in Software and Cyberinfrastructure for Astronomy IV, ed. G. Chiozzi & J. C. Guzman, Vol. 9913, International Society for Optics and Photonics (SPIE), 1232 – 1251, doi: 10.1117/12.2233418

Kilic, M., Gianninas, A., Bell, K. J., et al. 2015, The Astrophysical Journal Letters, 814, L31, doi: 10.1088/2041-8205/814/2/L31

Koch, D. G., Borucki, W. J., Basri, G., et al. 2010, The Astrophysical Journal, 713, L79, doi: 10.1088/2041-8205/713/2/l79

Kowalski, A. F., Hawley, S. L., Wisniewski, J. P., et al. 2013, The Astrophysical Journal Supplement Series, 207, 15, doi: 10.1088/0067-0049/207/1/15

Lacy, C. H., Moffett, T. J., & Evans, D. S. 1976, ApJS, 30, 85, doi: 10.1086/190358

Landstreet, J. D., & Bagnulo, S. 2019, A&A, 628, A1, doi: 10.1051/0004-6361/201936009

Landstreet, J. D., Bagnulo, S., Fossati, L., Jordan, S., & O'Toole, S. J. 2012, A&A, 541, A100, doi: 10.1051/0004-6361/201219178

Lomb, N. R. 1976, Ap&SS, 39, 447, doi: 10.1007/BF00648343

Lurie, J. C., Davenport, J. R. A., Hawley, S. L., et al. 2015, The Astrophysical Journal, 800, 95, doi: 10.1088/0004-637X/800/2/95

Maschberger, T., & Kroupa, P. 2009, Monthly Notices of the Royal Astronomical Society, 395, 931, doi: 10.1111/j.1365-2966.2009.14577.x

Maxted, P. F. L., O'Donoghue, D., Morales-Rueda, L., Napiwotzki, R., & Smalley, B. 2007, Monthly Notices of the Royal Astronomical Society, 376, 919, doi: 10.1111/j.1365-2966.2007.11564.x

Mendoza, G. T., Davenport, J. R. A., Agol, E., Jackman, J. A. G., & Hawley, S. L. 2022, The Astronomical Journal, 164, 17, doi: 10.3847/1538-3881/ac6fe6

Momany, Y., Zaggia, S., Montalto, M., et al. 2020, Nature Astronomy, 4, 1092, doi: 10.1038/s41550-020-1113-4

Mosteller, F., & Tukey, J. 1977, Data Analysis and Regression: A Second Course in Statistics, Addison-Wesley series in behavioral science (Addison-Wesley Publishing Company)

Namekata, K., Maehara, H., Honda, S., et al. 2021, Nature Astronomy, 6, 241, doi: 10.1038/s41550-021-01532-8

Paegert, M., Stassun, K. G., Collins, K. A., et al. 2021, arXiv e-prints, arXiv:2108.04778, doi: 10.48550/arXiv.2108.04778

Pál, A., Molnár, L., & Kiss, C. 2018, Publications of the Astronomical Society of the Pacific, 130, 114503, doi: 10.1088/1538-3873/aae2aa

Pashchenko, I. N., Sokolovsky, K. V., & Gavras, P. 2017, Monthly Notices of the Royal Astronomical Society, 475, 2326, doi: 10.1093/mnras/stx3222

Pedregosa, F., Varoquaux, G., Gramfort, A., et al. 2011, Journal of Machine Learning Research, 12, 2825

Pelisoli, I., Dorsch, M., Heber, U., et al. 2022, Monthly Notices of the Royal Astronomical Society, 515, 2496, doi: 10.1093/mnras/stac1069

Pettersen, B. R., & Hawley, S. L. 1989, A&A, 217, 187

Pietras, M., Falewicz, R., Siarkowski, M., Bicz, K., & Preś, P. 2022, The Astrophysical Journal, 935, 143, doi: 10.3847/1538-4357/ac8352

Richards, J. W., Starr, D. L., Butler, N. R., et al. 2011, The Astrophysical Journal, 733, 10, doi: 10.1088/0004-637x/733/1/10

Ricker, G. R., Winn, J. N., Vanderspek, R., et al. 2014, Journal of Astronomical Telescopes, Instruments, and Systems, 1, 1 , doi: 10.1117/1.JATIS.1.1.014003

Romero, A. D., Kepler, S. O., Hermes, J. J., et al. 2022, Monthly Notices of the Royal Astronomical Society, 511, 1574, doi: 10.1093/mnras/stac093

Salaris, M., Cassisi, S., Pietrinferni, A., & Hidalgo, S. 2021, Monthly Notices of the Royal Astronomical Society, 509, 5197, doi: 10.1093/mnras/stab3359

Saumon, D., Blouin, S., & Tremblay, P.-E. 2022, Physics Reports, 988, 1, doi: https://doi.org/10.1016/j.physrep.2022.09.001

Savitzky, A., & Golay, M. J. E. 1964, Analytical Chemistry, 36, 1627, doi: 10.1021/ac60214a047

Scargle, J. D. 1982, ApJ, 263, 835, doi: 10.1086/160554

Scaringi, S., Groot, P. J., Knigge, C., et al. 2022, Nature, 604, 447, doi: 10.1038/s41586-022-04495-6

Schaffenroth, V., Barlow, B. N., Pelisoli, I., Geier, S., & Kupfer, T. 2023, A&A, 673, A90, doi: 10.1051/0004-6361/202244697

Schaffenroth, V., Pelisoli, I., Barlow, B. N., Geier, S., & Kupfer, T. 2022, A&A, 666, A182, doi: 10.1051/0004-6361/202244214

Schmitt, J. H. M. M., Kahabka, P., Stauffer, J., & Piters, A. J. M. 1993, A&A, 277, 114

Shibayama, T., Maehara, H., Notsu, S., et al. 2013, The Astrophysical Journal Supplement Series, 209, 5, doi: 10.1088/0067-0049/209/1/5

Stassun, K. G., Oelkers, R. J., Paegert, M., et al. 2019, The Astronomical Journal, 158, 138, doi: 10.3847/1538-3881/ab3467

Sullivan, P. W., Winn, J. N., Berta-Thompson, Z. K., et al. 2015, The Astrophysical Journal, 809, 77, doi: 10.1088/0004-637X/809/1/77

Vida, K., Kővári, Z., Pál, A., Oláh, K., & Kriskovics, L. 2017, The Astrophysical Journal, 841, 124, doi: 10.3847/1538-4357/aa6f05

Vos, J., Pelisoli, I., Budaj, J., et al. 2021, A&A, 655, A43, doi: 10.1051/0004-6361/202140391

Švanda, M., & Karlický, M. 2016, The Astrophysical Journal, 831, 9, doi: 10.3847/0004-637X/831/1/9

Walkowicz, L. M., Basri, G., Batalha, N., et al. 2011, The Astronomical Journal, 141, 50, doi: 10.1088/0004-6256/141/2/50

Wenger, M., Ochsenbein, F., Egret, D., et al. 2000, Astron. Astrophys. Suppl. Ser., 143, 9, doi: 10.1051/aas:2000332

Woltjer, L. 1964, ApJ, 140, 1309, doi: 10.1086/148028

Wyrzykowski, Ł., Rynkiewicz, A. E., Skowron, J., et al. 2015, The Astrophysical Journal Supplement Series, 216, 12, doi: 10.1088/0067-0049/216/1/12

Wyrzykowski, Ł., Kostrzewa-Rutkowska, Z., Skowron, J., et al. 2016, Monthly Notices of the Royal Astronomical Society, 458, 3012, doi: 10.1093/mnras/stw426

Yang, H., & Liu, J. 2019, The Astrophysical Journal Supplement Series, 241, 29, doi: 10.3847/1538-4365/ab0d28

Yang, Z., Zhang, L., Meng, G., et al. 2023, A&A, 669, A15,
doi: 10.1051/0004-6361/202142710